https://doi.org/10.5194/egusphere-2026-3279
Preprint. Discussion started: 3 September 2026

Luminescence dating of offshore tsunami deposits from the Shetland Islands, United Kingdom

Andreas Peffeköver[1,2], Max Engel[3], Stephan Opitz[1], Anja Zander[1], Maarten Van Daele[4], Pedro J.M. Costa[5,6], Sue Dawson[7], Rikza N.F. An Nahar[4,8], Juliane Scheder[9], Vanessa M.A. Heyvaert[4,9], Marc De Batist[4], and Dominik Brill[1]

[1]Institute of Geography, University of Cologne, Cologne, Germany
[2]Department of Earth Sciences, Simon Fraser University, Burnaby, Canada
[3]Institute of Geography, Heidelberg University, Heidelberg, Germany
[4]Renard Centre of Marine Geology, Department of Geology, Ghent University, Ghent, Belgium
[5]Department of Earth Sciences, University of Coimbra, Coimbra, Portugal
[6]Instituto Dom Luiz, University of Lisbon, Lisbon, Portugal
[7]Energy, Environment and Society, University of Dundee, Dundee, Scotland
[8]Department of Geology, Faculty of Industrial Technology, Sumatera Institute of Technology, South Lampung, Indonesia
[9]Geological Survey of Belgium, Royal Belgian Institute of Natural Sciences, Brussels, Belgium

Correspondence to: Andreas Peffeköver (andreas_peffekover@sfu.ca)

Abstract. With onshore geological evidence of three tsunami events, the Shetland Islands (UK) yield the most-detailed Holocene tsunami record in the North Sea region. Lately, tsunami deposits were also identified in shallow waters offshore the Shetland Islands. These offshore tsunami deposits may carry the potential to further improve our understanding of both local and basin-wide, long-term tsunami hazard. Making use of the offshore record, however, requires establishing robust event chronologies. By using cores collected from two shallow-marine embayments located in the eastern Shetlands (Dury Voe and Colgrave Sound), we present the first chronology for offshore tsunami evidence from this region based on luminescence dating by resolving critical methodological challenges. The offshore cores show four distinct layers that contrast with the background shelf sediments. We find micro X-ray fluorescence mapping to be a rapid and effective method for assessing the geometries and internal architectures of these candidate tsunami deposits, which helps to guide sampling for luminescence dating. Complex radiation fields and time-dependency of environmental dose rates are tackled by implementing representative water contents, site-specific internal potassium contents, modeled dose rates considering the effect of radioactive disequilibria, and stratigraphic heterogeneity on the scale of gamma radiation. We demonstrate how robust luminescence-based chronologies can be achieved through measuring silt- and sand-sized K-feldspars with a $pIRIR_{130}$ protocol in combination with Bayesian age-depth modeling under these conditions. Our luminescence chronologies indicate sedimentary evidence of the Storegga tsunami at offshore Dury Voe and Colgrave Sound, and additionally of the late-Holocene tsunami at offshore Dury Voe. Overall, these results demonstrate both the great potential of luminescence dating for offshore tsunami deposits and the benefits of the associated chronologies for regional tsunami hazard assessment.

https://doi.org/10.5194/egusphere-2026-3279
Preprint. Discussion started: 3 September 2026

1 Introduction

Population growth and concentration of economic assets (Neumann et al., 2015) make coastal communities, infrastructures, and ecosystems highly vulnerable to both slow- (e.g., relative sea-level [RSL] rise) and rapid-onset natural hazards (storm surges or tsunamis) (Engel et al., 2020). Tsunamis are low-frequency high-magnitude events with recurrence intervals in the range of hundreds (e.g., Brill et al., 2012; Sawai et al., 2012) to several thousands of years (e.g., Costa et al., 2021a; Paris et al., 2018). Utilizing the sedimentary record allows to overcome the temporal limitation of short-term instrumental and historical records, and is thus of vital importance to assess site-specific long-term recurrence rates.

Sedimentary evidence indicates comparatively low recurrence rates of tsunamis in the North Sea region. The most prominent example of a tsunami is the 8150 cal. a BP Storegga event caused by a large submarine landslide at the Norwegian continental slope (Bondevik et al., 2005, 2012). The Storegga tsunami had a sedimentary imprint at numerous coastlines across the North Atlantic Ocean and the North Sea (Costa et al., 2021a for a summary). With onshore stratigraphic evidence of two additional Holocene tsunamis at 5500 cal. a BP and 1400 cal. a BP, the Shetland Islands (UK) yield the most-detailed tsunami record, and thus, became an important field laboratory for studying tsunami deposits in the North Sea region (Bondevik et al., 2005; Dawson et al., 2006, 2020; Engel et al., 2024; Nussberger et al., under review). However, as the completeness of onshore sedimentary records in the North Sea basin is constrained by low accommodation space and poor preservation potential (Costa et al., 2021a), both local and basin-wide tsunami risks may be still underestimated. Offshore tsunami deposits resulting from backwash are more likely to be preserved if deposited well below the storm-wave base (Schwarzer, 2020) and may therefore provide a more complete record of Holocene tsunami events.

Luminescence has proven to be an excellent method for dating tsunami deposits from modern to prehistorical times across a range of coastal settings worldwide (Brill and Tamura, 2020). Luminescence studies on Storegga tsunami deposits exist for a few coastal sites and settings around the North Sea (Bateman et al., 2021, 2022; Fruergaard et al., 2015; Gaffney et al., 2020). Only recently, Nussberger et al. (under review) presented the first luminescence ages of onshore tsunami deposits from the Shetland Islands, corroborating radiocarbon data and confirming the existence of a late-Holocene tsunami onshore at Dury Voe. Obtaining chronologies in marine and carbonate-rich environments is challenging (Li et al., 2021) and is believed to limit the use of luminescence dating in the offshore sector (Costa et al., 2021b). Until recently and in the context of offshore tsunami deposits, luminescence dating has been solely applied on shallow-marine background sedimentation above and below tsunami deposits (Goodman-Tchernov et al., 2009; Reinhardt et al., 2006). In a pioneering attempt, Brill et al. (2024) demonstrated that luminescence dating can provide robust offshore tsunami chronologies by dating actual tsunami sediments from the Algarve shelf in Portugal. However, applying luminescence dating to the offshore sediment record introduces severe geochronological complexities that demand novel applications and rigorous methodological validation.

Our study presents the first attempt at luminescence dating offshore tsunami deposits and shelf sediments from the Shetland Islands. Thereby, our study directly contributes to finding solutions for challenges in dating young offshore event deposits. We use sediment cores from two shallow-marine embayments, Dury Voe and Colgrave Sound, both located on the eastern

https://doi.org/10.5194/egusphere-2026-3279
Preprint. Discussion started: 3 September 2026

coast, facing the North Sea. The post-glacial sedimentary evolution and stratigraphy of these embayments were recently studied by An Nahar et al. (under review), who found high-amplitude, laterally continuous seismic units with sharp erosional bases and shell-rich, poorly sorted lithologies that they linked to regionally extensive tsunami events.

Our study aims to establish luminescence-based chronologies by dating the silt and sand fractions of these candidate offshore tsunami deposits and their bracketing shelf sediments. To guide sample collection, we applied micro X-ray fluorescence (µXRF) mapping to reveal the internal architecture of the candidate tsunami deposits and to discriminate them from *in-situ* shelf sedimentation. For assessing dose rates in this challenging environment, we i) estimated facies-related representative water contents by using saturation experiments, ii) determined site-specific internal potassium contents by means of scanning electron microscopy with energy-dispersive X-ray spectrometry (SEM-EDX) and low-level beta counting, and iii) considered the effect of radioactive disequilibria in the uranium (U) decay chain by a combination of mass spectrometry and dose rate modeling. The resulting potassium (K-)feldspar luminescence chronologies were refined through Bayesian age-depth modeling.

By using this multi-methodological toolbox, we demonstrate the applicability of luminescence for dating Holocene offshore tsunami and shelf deposits from the Shetland Islands and establish a transferrable framework for future studies dating offshore tsunami deposits by means of luminescence. The new data shall be used to independently verify or even extend the existing chronologies of the regional tsunami record, which until recently was only based on onshore deposits mainly dated with radiocarbon. Ultimately, the new chronologies will contribute to an improved understanding of the regional and long-term tsunami hazard for the Shetland Islands and, more broadly, the coastline of northwestern Europe.

2 Study area

2.1 Physical setting

The Shetland Islands (Scotland, UK; 1°W, 60°N) are a north-south oriented archipelago of >100 islands situated at the northern margin of the North Sea (Fig. 1). They are a terrestrial expression of the much larger Orkney-Shetland Platform which is part of the Caledonian Orogenic belt. It extends from northeast Scotland and represents a southwest-northeast-directed topographical, bathymetrical, and hydrographic divide separating the temperate waters of the North Atlantic to the west from the cooler waters of the North Sea to the east (Bradwell et al., 2019; Hall et al., 2021). This tectonic framework is demonstrated by the regional formation of terranes in combination with mainly north-south directed strike-slip faults (Watts et al., 2007) and small-scale thrusts resulting in a complex pattern of metamorphic and igneous bedrock (Hall et al., 2021).

Present-day geomorphology is strongly influenced by repeated cycles of northern-hemisphere glaciation and deglaciation during the Pleistocene (Batchelor et al., 2019). During the Last Glacial Maximum (LGM) the Shetland Islands' ice cap covered large parts of its present-day land surface and continental shelf (Bradwell et al., 2019; Graham et al., 2011). Glacial erosion during cold stages led to the incision of valleys that were drowned during subsequent late-glacial and early-Holocene RSL rise, ultimately leading to the formation of fjords. These sheltered embayments, locally called voes, are characteristic for the

https://doi.org/10.5194/egusphere-2026-3279
Preprint. Discussion started: 3 September 2026

Shetlands' low-energy inner coastal environments whereas much of the outer coastline comprises cliffs exposed to high-energy conditions.

Down to the present day, accurate Holocene RSL data for the Shetlands is scarce (Engel et al., 2024) and the majority of existing reconstructions are based on modeling approaches with very few local sea-level index points involved. Current estimates indicate that RSL was ~34–27 m below present mean sea level (msl) during the Storegga tsunami, ~12–9 m below present msl during the mid-Holocene tsunami, and ~1 m below present msl during the late-Holocene tsunami (An Nahar et al., under review; Bondevik et al., 2005; Dawson et al., 2020). Glacio-isostatic adjustment models for the North Sea synchronously highlight that the RSL rose rapidly until the mid-Holocene, started to flatten, and then stabilized during the late Holocene and kept rising at a low rate (Bradley et al., 2011; Kuchar et al., 2012; Shennan et al., 2018). Instrumental records show no trend in local RSL since the mid-20th century (Wahl et al., 2013).

2.2 The regional and local tsunami hazard

2.2.1 Holocene tsunami occurrence in the North Sea region

The North Sea coastline indicates comparatively low recurrence rates of tsunami events in the Holocene. Since the end of the Pliocene, a series of submarine landslides occurred on the passive margin west of Norway, referred to as the Storegga slides, with an estimated recurrence frequency of 100 ka over the last 0.5 Ma (Bryn et al., 2005; Solheim et al., 2005), although the actual number might be higher based on recent discoveries (Karstens et al., 2023). Its most-recent slide (Fig. 1a) took place in the early Holocene and triggered the largest known tsunami in the North Sea basin, referred to as the Storegga tsunami (8120–8175 cal. a BP; Bondevik et al., 2012), which affected the coasts of northern and northwestern Europe (Haflidason et al., 2005). It is one of the rare examples where large submarine landslides generated mid- to far-field and even basin-wide tsunamis, far away from active plate margins. Sedimentary evidence of the Storegga tsunami is found in various onshore settings such as coastal lakes (e.g., Rasmussen et al., 2018), estuaries (e.g., Dawson and Smith, 2000), coastal embayments (e.g., Tooley and Smith, 2005) or shelf environments (An Nahar et al., under review; Earland et al., 2024) of England (e.g., Hill et al., 2017), Scotland (e.g., Long et al., 1989), the Faroe Islands (Grauert et al., 2001), the Shetland Islands (e.g., Bondevik et al., 2005), Denmark (Fruergaard et al., 2015), Norway (e.g. Romundset and Bondevik, 2011), Greenland (Wagner et al., 2007) (Fig. 1a) and as far as the Barents Sea (Devendra et al., 2025).

2.2.2 Evidence of tsunami events in the Shetland Islands

Bondevik et al. (2003, 2005) were able to assign a previously documented anomalous deposit from Garth Voe (Birnie, 1981; Smith, 1993) to the Storegga tsunami and attributed other sand layers, e.g. at Maggie Kettle's Loch (Sullom Voe, Mainland), to the event. Another well-preserved Storegga tsunami deposit was reported at Whale Firth (Yell) by Dawson et al. (2020). Deposits attributed to the Storegga tsunami reach elevations of up to 11.8 m above present mean sea level at Scatsta Voe, Mainland (Smith et al., 2004). Combined with regional RSL reconstructions, these observations suggest local runup heights

https://doi.org/10.5194/egusphere-2026-3279
Preprint. Discussion started: 3 September 2026

exceeding 38 m, although such estimates are not fully supported by recent tsunami modeling results of corresponding wave heights reaching merely 13 m (Dawson et al., 2020).

Bondevik et al. (2005) also discovered a potential mid-Holocene tsunami deposit, dated to 5500 cal. a BP and referred to as the Garth tsunami, in the record of two freshwater coastal lakes, Loch of Benston and Garth Loch (Mainland). Runup heights of the mid-Holocene tsunami were inferred to be much lower than those of the Storegga tsunami (Bondevik et al., 2005). Even though efforts have been made (Bondevik et al., 1997, 2005; Romundset et al., 2015), there is no unequivocal sedimentary evidence of this mid-Holocene tsunami outside the Shetlands, and its trigger is unclear. Cain et al. (2019) tentatively linked human mass-burial sites in the Orkneys and the Shetlands to the Garth tsunami, although no new empirical evidence was presented. Based on an archaeological hiatus in the 4th millennium BC at sites in western Norway, Nielsen (2020) proposes the Garth tsunami to have had a strong impact on hunter-fisher-gatherer populations. In the absence of age control and a confirmed trigger, however, the existence and extent of the Garth tsunami remain debatable.

A third deposit of potential tsunamigenic origin, referred to as the Dury Voe tsunami, was discovered by Bondevik et al. (2005) in Dury Voe (Mainland) and by Dawson et al. (2006) in Basta Voe (Yell). Recently, further evidence of the late-Holocene tsunami was presented by Engel et al. (2024) in the coastal lake of Loch Flugarth, located in the northwestern Shetlands. Based on reinterpreting and adding chronological data, Engel et al. (2024) suggested a refined timing of 1400 cal. a BP, recently confirmed by luminescence ages from Dury Voe (Nussberger et al., under review). The trigger and source of the late-Holocene tsunami remain unclear to the present day. Both Bondevik et al. (2005) and Dawson et al. (2006) suggested the Dury Voe tsunami to be a local phenomenon, potentially triggered by a slump offshore of the eastern Shetlands, whereas specific geophysical evidence is absent (Long, 2015).

2.3 Sampling sites

The embayments of Dury Voe and Colgrave Sound/Basta Voe are situated on the eastern coastline of the Shetland Islands, facing the North Sea (Fig. 1b). Dury Voe comprises a series of coastal inlets which are located in the northeast of the Shetlands' biggest island, Mainland. The main inlet of Dury Voe leads to the Ayre of Dury, a pebble beach with peat outcrops where the 1400 cal. a BP tsunami was first described as a distinct thin sand layer (Bondevik et al., 2005). Bathymetric data of the study area and its surroundings reveal a heterogeneous and rugged seafloor morphology highlighted by the occurrence of submarine bedrock peaks in an overall shallow-marine setting (water depths <80 m) (An Nahar et al., under review) (Fig. 1c).

Colgrave Sound is a funnel-shaped embayment located to the east of Yell. To the north, it is delimited by the Island of Hascosay, separating the sound from Basta Voe to the north, which represents the tip of the funnel shape. The western coast of Basta Voe exposes low peat cliffs with outcrops containing a sand layer of the late-Holocene tsunami interbedded within peat overlying glacial deposits (Bondevik et al., 2005; Dawson et al., 2006). The ocean-floor morphology is fairly smooth (water depths ranging from <10 m in Basta Voe to 90 m in Colgrave Sound) (An Nahar et al., under review) with the small island of Hascosay representing a subaerial peak within the greater study area and the larger island of Fetlar sheltering Colgrave Sound to the east (Fig. 1d).

https://doi.org/10.5194/egusphere-2026-3279
Preprint. Discussion started: 3 September 2026

Earland et al. (2024) collected sediment cores at a water depth of 116 m in the Fetlar Basin that revealed distinct sand and shell lenses within a Holocene mud sequence, indicating a sudden change in hydrodynamic conditions during tsunami impact. Radiocarbon dates bracketing these sand lenses overlap with the Storegga event and radiocarbon ages within the deposit were older. No evidence of younger Holocene tsunamis was found in the sediment cores (Earland et al. 2024). Most recently, An Nahar et al. (under review) presented a seismic-stratigraphic reconstruction of post-glacial sedimentation in both Dury Voe and Colgrave Sound/Basta Voe. They found four main stages of post-glacial deposition: (i) a pre-marine substrate of crystalline bedrock locally mantled by glacial or glaciofluvial deposits; (ii) early post-glacial infill deposited under low-energy, restricted conditions within isolated or semi-restricted basins in fluvial, lacustrine, or estuarine environments; (iii) a transitional phase associated with the early Holocene marine transgression and increasing hydrodynamic influence; and (iv) an upper succession dominated by sand-rich, current-influenced marine deposits forming laterally extensive mounded drift geometries. They further reported laterally continuous seismic units with sharp erosional bases and shell-rich, poorly sorted lithologies pointing to extreme-wave events. Radiocarbon dating links the older event deposit with the Storegga tsunami and the younger event deposit to the late-Holocene tsunami (An Nahar et al., under review).

https://doi.org/10.5194/egusphere-2026-3279
Preprint. Discussion started: 3 September 2026

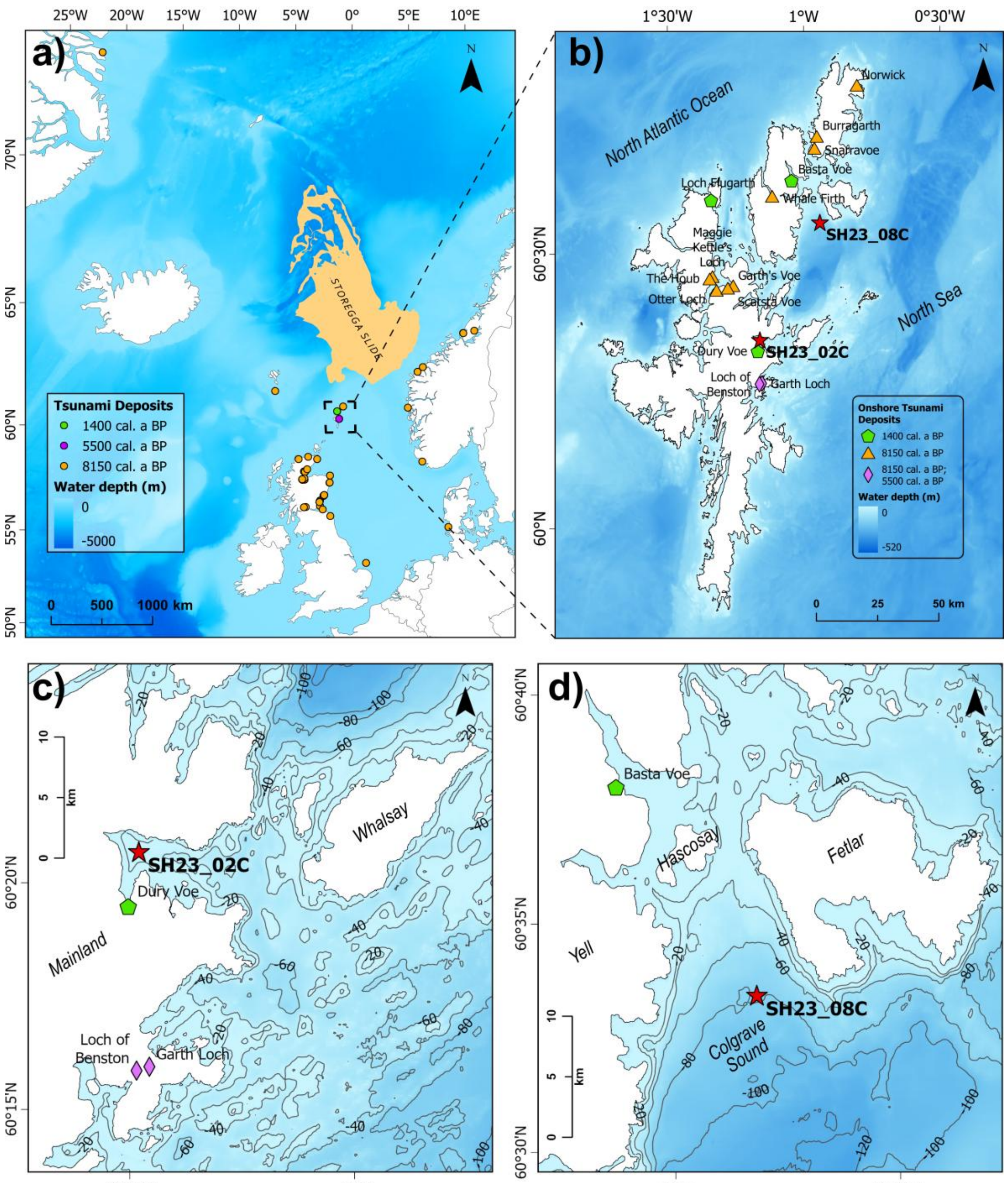

Figure 1: Study area with locations of known onshore tsunami deposits and offshore sediment cores of this study. a) North Atlantic and North Sea basin with locations of published tsunami deposits. b) Locations of known onshore tsunami deposits on the Shetland Islands and core locations of this study. c) Core location, onshore tsunami deposits, and bathymetry at Dury Voe. d) Core location, onshore tsunami deposits, and bathymetry at Colgrave Sound/Basta Voe. Bathymetric data are derived from General Bathymetric Chart of the Oceans (GEBCO) 2025 grid (GEBCO Compilation Group, 2025). All spatial data were projected using the WGS 1984 geographic coordinate system.

https://doi.org/10.5194/egusphere-2026-3279
Preprint. Discussion started: 3 September 2026

3 Material and methods

3.1 Fieldwork and core correlation

Fieldwork was conducted aboard *Research Vessel (RV) Belgica* in September 2023 as part of the NORSEAT ("Storegga and beyond – NORth SEA Tsunami deposits offshore Shetland Islands") project. Fieldwork included offshore coring with a 4.5 m OSIL high-power vibrocorer using opaque PVC liners (Van Daele et al., 2023). Coring sites were selected based on preliminary interpretation of the sub-bottom and bathymetric data (An Nahar et al., under review). At 19 of the 31 coring sites, three cores (A-, B-, and C-cores) were recovered from individual boreholes located a few meters apart.

Two of the sediment cores from the shelf at the east coast of the Shetland Islands, i.e., SH23-02C (Dury Voe, parallel core to SH23-02 in An Nahar et al. under review) and SH23-08C (Colgrave Sound, parallel core to SH23-08 in An Nahar et al. under review) (Fig. 1b), were chosen for this study. The Dury Voe core (60°20.684'N, 001°09.592'W) was taken at 36 m below msl (Fig. 1c). The Colgrave Sound core (60°33.445'N, 000°56.396'W) was retrieved at 81 m below msl (Fig. 1 d). Cores were split under subdued red-light conditions in the Cologne Luminescence Laboratory (CLL). One half of each core was used for core logging and µXRF mapping in the Physical Geography Laboratory at Cologne University, the other half for luminescence dating.

To guide sample collection, both cores used in this study were correlated with the existing stratigraphies (An Nahar et al., under review) using visual descriptions of sediment facies. Based on this correlation, we collected samples for µXRF analyses from candidate tsunami events and for luminescence dating both from event layers and background sediments directly above and below.

3.2 µXRF for candidate tsunami deposits

µXRF mapping was used to determine the contacts between high-energy event deposits and low-energy background sedimentation, guiding the sampling strategy for luminescence samples. Based on Chagué (2020) and the conditions of the local sedimentary environments, we assumed that Mn, Fe, Si, and Ti are associated with beach or terrestrial environments. In contrast, Na, S, and Br are assumed to be associated with seawater, Ca and Sr with the presence of biogenic carbonates, and thus, both with marine environments. For µXRF measurements, candidate tsunami deposits were sub-sectioned based on visual observations following core logging. Afterwards, ~2 cm of sediment was carefully removed from the exposed core surface to avoid potential disturbances caused by cutting and slicing. Segments were surface-cleaned, leveled, and dried at 50 °C for one week. Prior to µXRF mapping, precipitated salt was removed from the surface with a single-cut metal file to prevent elemental artefacts. High-resolution measurements in 40 µm intervals and with a measurement time of 25 ms were performed using a two-detector Bruker M4 Tornado system equipped with a rhodium anode, operating at 50 kV and 300 µA. Mass fractions of 15 elements (Na, Al, Si, S, Cl, K, Ca, Ti, V, Mn, Fe, Br, Rb, Sr, Zr) were determined under controlled vacuum conditions at 20 mbar to enhance sensitivity for light elements. The X-ray beam was focused by a polycapillary lens with a spot size of ~20 µm. µXRF results were exported as images contrasting two non-quantified, color-coded elements.

https://doi.org/10.5194/egusphere-2026-3279
Preprint. Discussion started: 3 September 2026

3.3 Luminescence dating

Since tests on both cores revealed inappropriate quartz luminescence properties (S1, Fig. S1), we used multi-grain (MG) and single-grain (SG) aliquots of sand-sized K-feldspar and fine-grain (FG) polymineralic extracts for luminescence dating. A summary of which dosimeter was measured for which sample is shown in Table S2.

3.3.1 Sample preparation and measurement equipment

Subsampling and sample preparation for luminescence dating were conducted under subdued red-light conditions. Samples underwent chemical treatment including a sequence of hydrochloric acid (HCl, 10%), hydrogen peroxide (H_2O_2, 10%), and sodium oxalate ($Na_2C_2O_4$, 0.01 N) to remove carbonates, organic material, and aggregates, respectively. Subsequently, samples were sieved to divide them into their fine- and coarse-grain fractions, where possible. Polymineralic fine-grain samples of 4–11 µm were isolated using density settling and a centrifuge. Coarse-grain samples were dry sieved in order to isolate the 100–250 µm fraction. Density separation using sodium polytungstate ($3\ Na_2WO_4 \cdot 9\ WO_3 \cdot H_2O$) was applied to separate K-feldspar (ρ <2.58 g/cm³). Whenever possible, coarse-grain K-feldspars were sieved in smaller fractions of 100–150 µm, 150–200 µm, and 200–250 µm. For MG measurements, either 1, 2, or 4 mm patches of coarse-grain K-feldspars were fixed on stainless steel discs using silicon spray. For SG measurements, coarse-grain K-feldspars were brushed into either 200 µm, 250 µm, or 300 µm diameter holes of standard SG discs. Fine-grain minerals were suspended in demineralized water (5.0 mg/ml), pipetted on steel discs, and dried at 50 °C prior to measuring.
Luminescence measurements were performed on automated Risø TL/OSL DA20 readers equipped with $^{90}Sr/^{90}Y$ beta sources delivering a dose rate of ~0.09 (MG and FG measurements) – 0.12 Gy/s (SG measurements) at the sample position. The beta sources were calibrated using Risø calibration quartz. Dose rates of the instruments were determined by fitting a regression line through multiple calibrations, with the instruments being calibrated every 6 months. MG signals were stimulated with infrared LEDs (850 nm, 300 mW/cm², 90% power) and detected through a combination of 2 mm Schott BG39 and AT405/30x interference filters. SG luminescence measurements were stimulated with an IR laser (830 nm, 500 mW/cm²) for 2 s and detected through a blue filter pack (Schott BG39 + Schott BG3).

3.3.2 Paleodose determination

To find a suitable measurement protocol we tested different post-infrared-infrared-stimulated luminescence (pIRIR) procedures (e.g., Buylaert et al., 2009; Reimann and Tsukamoto, 2012). After preheating for 60 s (we tested six different temperatures between 160 °C and 320 °C), a first IR signal was measured for 200 s at 50 °C (IR_{50} signal), followed by a post-IR signal measured at 25 °C or 30 °C below the preheat temperature (pIRIR signal, 130 °C to 290 °C) for 300 s (Dury Voe [DUVO]) or 500 s (Colgrave Sound/Basta Voe [BAVO]). All test measurements were performed on three MG aliquots of K-feldspar per temperature combination for one sample of each core. Tests included a dose-recovery preheat plateau test and a residual preheat plateau test, both after 24 h of bleaching in a Dr. Hönle SOL2 solar simulator. Additionally, as K-feldspars may be affected by anomalous fading, fading rates (i.e., g-values as %/decade) were measured by applying the approach of Auclair et al. (2003) with storage times of 10, 100, and 1000 min after irradiation. Based on these test measurements, a $pIRIR_{130}$ protocol was chosen and validated for all remaining samples by means of dose recovery tests, residual dose measurements, and fading tests using three MG K-feldspar aliquots.

The $pIRIR_{130}$ protocol was applied for equivalent dose (D_e) measurements of the silt-sized polymineralic, as well as of the sand-sized K-feldspar samples (Table S3). Acceptance criteria for all measured MG aliquots and SGs for both the IR_{50} and $pIRIR_{130}$ signal were defined as exhibiting a recycling ratio within 10% of unity, a maximum test dose error of 10%, and a test dose signal with intensities of more than 3 σ above background. Additionally, for the IR_{50} signal, a maximum recuperation of 5% compared to the largest regeneration dose was set as a criterium. Exponential curve fitting was chosen to build dose response curves. After applying the rejection criteria, dose distributions are based on 10 (polymineralic), or 16–24 (K-feldspar) MG aliquots and 10–168 SGs per sample.

Paleodoses for the silt-sized polymineralic fraction, for which overdispersion of the accepted aliquots remained below 5%, were calculated using the central age model (CAM; Galbraith et al., 1999). The majority of D_e measurements of coarse-grain samples showed normal distributions and paleodoses were therefore calculated using the CAM. For D_e distributions with larger overdispersion values, paleodoses were calculated with either the minimum age model (MAM; Galbraith et al., 1999) in case of right-skewed D_e distributions, or the finite mixture model (FMM; Galbraith, 2005) in case of multi-populational D_e distributions. The σ_b parameter required for paleodose calculation with the MAM and the FMM was estimated for each aliquot size (SG, MG) and signal (IR_{50}, $pIRIR_{130}$) separately by using the approach of Chamberlain et al. (2018). Statistics including D_e distributions, dose models, and plots were performed using the *Luminescence* package by Kreutzer et al. (2012) in the *R studio* software version 2025.09.2.

3.3.3 Dose rate assessment and age calculation

External dose rates were measured on eight and seven bulk samples for Dury Voe and Colgrave Sound, respectively, by means of high-resolution gamma-ray spectrometry using an Ortec Profile M-Series GEM Coaxial P-type high-precision Ge gamma-ray detector. Specific activities and contents of ^{238}U, ^{232}Th, and ^{40}K were determined as the main contributors to external dose rates. Prior to measurement, samples were dried, homogenized, and, based on sediment availability, amounts of either ~40 g or ~200 g were stored in airtight polystyrol containers for a minimum of four weeks to compensate for radon loss during sample preparation. In order to investigate disequilibria in the U decay chain, additional measurements using gamma-ray spectrometry, inductively coupled plasma mass spectrometry (ICP-MS) as well as alpha spectrometry were conducted at the VKTA – Strahlenschutz, Analytik & Entsorgung Rossendorf e.V. on three representative samples. These provided more robust values for the activity of individual nuclides within the U and Th decay chains including ^{234}Th for ^{238}U, ^{214}Pb and ^{214}Bi for ^{226}Ra, ^{228}Ac for ^{228}Ra, ^{212}Pb and ^{208}Tl for ^{228}Th. The specific activity for ^{232}Th is the weighted average of the values for ^{228}Ra and ^{228}Th and was calculated under the assumption that the ^{232}Th decay series is in secular equilibrium. The element concentration of U was calculated from the specific activity of its daughter nuclide ^{234}Th under the assumption that a

https://doi.org/10.5194/egusphere-2026-3279
Preprint. Discussion started: 3 September 2026

radioactive equilibrium exists between ^{238}U and this nuclide. The element concentration of Th was calculated from the specific activity of ^{232}Th.

Moisture content is an essential parameter for luminescence dating. Water attenuates ionizing radiation, and thus, influences dose rates (Mahan et al., 2022). Underestimations of water content cause overestimations of dose rates and, therefore, underestimations of corresponding ages (Murray et al., 2021). Water contents for luminescence dating are commonly determined through water loss after drying (i.e., gravimetric water content, further referred to as measured water content). Samples of this study originate from marine settings, hypothesized to be water-saturated at least since the early Holocene (An Nahar et al., under review). As loss of water was observed during core splitting, resulting water contents derived from the common approach may not represent *in-situ* values. To compensate for that, additional water saturation contents were measured for representative sedimentary facies of both cores by subsampling ~100 cm^3 of sediment using a steel cylinder with a water-permeable filter on one end. Samples were placed in a beaker, gradually filled with water and left for a few hours. Water saturation was defined as the state where visible uptake of water from the beaker ceased. Water contents were measured through gravimetric mass comparisons of water-saturated and dry sediment.

For luminescence dating using K-feldspar, ionizing radiation partly results from the internal decay of K within the mineral. Most K-feldspar luminescence studies make use of internal K contents derived from literature such as 10 ± 2% (Smedley et al., 2012) or 12.5 ± 2% (Huntley and Baril, 1997). However, recent findings of Maßon et al. (2025) highlight the variability of internal K contents for specific sediments. Therefore, site- and layer-specific internal K contents were obtained through a combination of low-level beta counting and SEM-EDX. Low-level gas-flow (99% Ar/1% isobutane) beta counting was conducted on all 15 luminescence samples using a Risø Geiger-Mueller (GM)-25-5 beta counter (Bøtter-Jensen and Mejdahl, 1985). Samples were prepared after Bøtter-Jensen and Mejdahl (1988). Each 100 mg of isolated K-feldspar was placed on upturned plastic pots and fixed with plastic wrap. Pots were inserted into the counter with the thin plastic film on the upper surface directed to the GM detector. Each sampling position was calibrated with ^{36}Cl (1 min per position) before measuring. Measurement specifications included usage of two known-activity standards (FK-N 2 and FK N-3), one no-activity standard (sucrose ($C_{12}H_{22}O_{11}$)) for background signals, and two unknown-activity pots of the same sample. Beta counting for each sample was performed in cycles of 60 min for 24 h. Beta activities were calculated by comparing the beta count rate from unknown samples with the count rate from the known-activity standards. Beta activities given in counts were translated into K_2O concentrations which were then converted into K contents using a factor of 1.21.

SEM-EDX was conducted at the Institute of Geology and Mineralogy at the University of Cologne on isolated K-feldspars for two samples per core. In order to account for potential differences in sediment source areas, one sample was chosen from shelf background sedimentation and one from allochthonous tsunami deposits. For each sample, ~100 grains were brushed into 300 µm diameter holes of a SG disc. A glass microscope slide with double-sided sticky tape was placed on top of the SG disc. Grains were transferred onto the tape by turning the slide and tapping on the backside of the disc with a piezoelectric ultrasonic cleaner (vibration frequency 30 ± 3 kHz). Prior to SEM-EDX measurements, the grains were bedded in transparent two-component Araldite 2020 Huntsman epoxide resin. After solidifying, surfaces were sanded with a 1200 SiO_2 sandpaper and

https://doi.org/10.5194/egusphere-2026-3279
Preprint. Discussion started: 3 September 2026

polished to remove potential epoxide cover from grains. The major element geochemical composition was determined grain by grain on a Zeiss Sigma 300-VP SEM with an EDX attachment. Measurement specifications included a working distance of 8.5 mm, an aperture diameter of 60 µm, an accelerating voltage of 20 kV, and a pixel spot size of ~2.2 µm (corresponding to a resolution of 512 x 384 pixels), which resulted in an output count rate of ~45,000 cps. Stoichiometry was used to determine individual chemical compositions of feldspar grains for the nine elements O, Na, Mg, Al, Si, K, Ca, Ti, and Fe. Eventually, sample-specific internal K contents were determined using mean K values of all individual grains that contained K-feldspar.

Dose rate and age calculations were performed in *ADELEv2017* (Degering and Degering, 2020). Conversion factors for gamma and beta dose rates were taken from Guérin et al. (2011), alpha grain-size attenuation factors from Brennan et al. (1991) and beta grain-size attenuation factors from Brennan (2003). Alpha efficiency values of 0.07 ± 0.01 (IR_{50}) and 0.11 ± 0.01 ($pIRIR_{130}$) (Kreutzer et al., 2014) were used to correct the alpha contribution to the total dose rate. Cosmic dose rate calculations in dependence of geographical setting based on Prescott and Hutton (1994) were conducted. For shielding, paleo-sea-level conditions were estimated based on existing Holocene RSL reconstructions for the North Sea (Bradley et al., 2011; Shennan et al., 2018) and an overburden density of 1.8 g/cm³ for sediment. Gamma dose-rate heterogeneity was considered using a layer model according to Aitken (1985). Eventually, K-feldspar ages (both IR_{50} and $pIRIR_{130}$) were corrected for anomalous fading using the approach of Huntley and Lamothe (2001).

For considering the effect of disequilibria in the U decay chain, three separate dose rates were calculated: (1) a minimum dose rate (DR_{min}) based on ^{238}U concentrations derived from gamma-ray spectrometry; (2) a maximum dose rate (DR_{max}) based on ^{226}Ra concentrations measured by gamma-ray spectrometry; (3) a modeled dose rate (DR_{mod}) based on changing U activities over time. For each scenario, facies-specific effective water contents derived from saturation experiments (30 ± 10% for sand layers, ≤66 ± 10% for shelf deposits), were compared with measured water contents for sensitivity assessment. To investigate the sensitivity regarding internal K content, site-specific values of 7.0 ± 2.0% (Dury Voe) and 5.3 ± 2.0% to 10.0 ± 2.0% (Colgrave Sound) were compared with literature values.

3.4 Age-depth modeling

To further refine the luminescence chronologies, Bayesian age-depth modeling was applied separately for each core using the Poisson Process depositional model (P_Sequence) in OxCal version 4.4 (Bronk Ramsey, 2009). Luminescence dating results (IR_{50} and $pIRIR_{130}$ ages for Dury Voe; IR_{50} for Colgrave Sound) were integrated into the models to provide a continuous age-depth relationship from the base to the top of each core (Table S11). *k* parameters of 1 and interpolation values of 0.1 (corresponding to interpolation at every 10 cm) were utilized to allow for flexible yet stratigraphically consistent accumulation rates. To account for instantaneous deposition of event layers, multiple luminescence ages within candidate event deposits were defined as one depositional phase. The implementation of luminescence ages into OxCal was based on age probability distributions provided by the aforementioned dose models. For this, dose probability distributions provided by the dose models were transformed into age distributions by dividing paleodoses through the associated dose rate DR_{mod} and correcting for fading in case of IR_{50} ages for both cores, and additionally for $pIRIR_{130}$ ages for Colgrave Sound. All age inputs were entered as absolute years before 2023 (i.e., year of sampling) with their age errors, and the SD1 option was enabled to identify potential outliers. All ages were modeled including their total propagated errors, ensuring that the posterior probability ranges remain conservative and do not artificially compress the age-depth boundaries. We did not exclude systematic uncertainties shared between the samples of individual cores prior to the calculations in OxCal as proposed by Rhodes et al. (2003), because these (i.e. beta source error and uncertainties of dose rate conversion factors) had insignificant values <1% of the final dating uncertainties for our dataset compared to the relatively large uncertainties related to water contents and interpolation of luminescence signals onto dose-response curves. Final age estimates for both cores are reported based on the 68.3% probability range (1 σ) of the posterior distribution.

4 Results and interpretation

4.1 Facies succession, geometry of candidate event layers, and sampling scheme

By correlation of cores SH23-02C (Dury Voe) and SH23-08C (Colgrave Sound) with parallel cores discussed by An Nahar et al. (under review) using core-to-seismic correlation, the succession of depositional environments is established (Fig. 2). Combined with µXRF-based information regarding the geometry and internal architecture of the identified candidate tsunami layers (Fig. 3), this stratigraphy provides the basis for the sampling scheme for luminescence dating.

4.1.1 Dury Voe

The basal facies (91–283 cm below the sediment surface [b.s.]) of SH23-02C consists of well-sorted silt- to sand-sized sediments that are interrupted by a slightly coarser unit (DV2, 221–228 cm b.s.), which exhibits coarser sand lenses and larger (~5 cm in diameter) shell fragments compared to the surrounding deposits (Fig. 2a). Terrestrial-associated elements (Mn, Fe, Ti) are ubiquitous in this basal facies and DV2 (Fig. 3c). Plotting elements of biogenic carbonates (Ca, Sr) against terrestrial elements shows an overall chaotic alignment of carbonates (i.e., shell fragments) interbedded in a terrestrial-dominated background signal. The µXRF images highlight sharp upper and lower depositional boundaries. Based on stratigraphic observations and µXRF characteristics, DV2 is a candidate event deposit. Luminescence samples are taken from the candidate event deposit itself (DUVO-6, 225–226 cm b.s.), as well as right below (DUVO-7, 232–233 cm b.s.) and above (DUVO-5, 217–218 cm b.s.) in slightly finer-grained background sedimentation (Fig. 2a).

The overlying facies (24–91 cm b.s.) shows moderately sorted sand-dominated sediments with abundant small- to medium-sized (max. 2 cm in diameter) shell fragments. These sediments are interrupted by layer DV1 (45–56.5 cm b.s.), which reveals a sharp basal contact and a gradual upper boundary (Fig. 2a). DV1 is normally graded and consists of coarse sand that fines into medium sand towards the top. It is enriched in terrestrial-associated elements (Mn, Fe, Ti) compared to the marine-dominated (Na, S, Br) background sedimentation (Fig. 3a). The visually distinct basal contact of DV1 is slightly blurred in the µXRF imagery, whereas the upper boundary shows distinct elemental changes. Based on these features, DV1 is another candidate event deposit. Luminescence samples are collected from right below the basal contact at 58–59 cm b.s. (DUVO-4),

https://doi.org/10.5194/egusphere-2026-3279
Preprint. Discussion started: 3 September 2026

from the coarser-grained (DUVO-3, 53–54 cm b.s.) and finer-grained (DUVO-2, 47–48 cm b.s.) section within DV1, and from above DV1 (DUVO-1, 39–40 cm b.s.). The uppermost facies (0–24 cm b.s.) consists of organic-rich sandy silt with occasional small- to medium-sized (max. 2 cm in diameter) shells and shell fragments.

4.1.2 Colgrave Sound

The basal facies (160–165 cm b.s.) of SH23-08C is poorly sorted and consists of a fine sand matrix, well-rounded gravel, and abundant larger (~5 cm in diameter) shells and shell fragments, from which one luminescence sample (BAVO-8, 160–165 cm b.s.) is collected to determine a basal age of the core. It is overlain by silt-dominated sediments (117–160 cm b.s.) that are almost entirely free of shells and shell fragments. This is followed by a coarse-grained and normally graded sand layer (BV2, 102–117 cm b.s.) with abundant shell fragments (max. 1 cm in diameter) (Fig. 2b). µXRF data visualize a sharp basal contact and a slightly less distinct upper contact (Fig. 3e). BV2 shows Ca- and Si-rich components, while the surrounding sediments are marked by terrestrial-associated elements (Fe, Mn), making it a candidate event deposit. Luminescence samples are taken from background sediments right below (BAVO-7, 117–119 cm b.s.) and above (BAVO-4, 103–105 cm b.s.), as well as from the coarser-grained (BAVO-6, 114–116 cm b.s.) and the finer-grained sections (BAVO-5, 106–108 cm b.s.) within BV2.

The facies overlying BV2 (58–102 cm b.s.) exhibits moderately sorted fine sand with varying concentrations of shell fragments and high amounts of mica. The uppermost facies (0–58 cm b.s.) of the Colgrave Sound core shows poorly sorted bioclastic sand with abundant smaller-sized (mm-scale) shell fragments. It is interrupted by a slightly coarser unit (BV1, 14–17 cm b.s.) which consists of larger (max. 1 cm in diameter) shell fragments and shows a lighter color, but more gradual lower and upper boundaries. Nevertheless, BV1 is another candidate event. To bracket BV1, luminescence samples are collected from upper (BAVO-1, 10–13 cm b.s.) and lower (BAVO-2, 18–22 cm b.s.) background sedimentation.

https://doi.org/10.5194/egusphere-2026-3279
Preprint. Discussion started: 3 September 2026

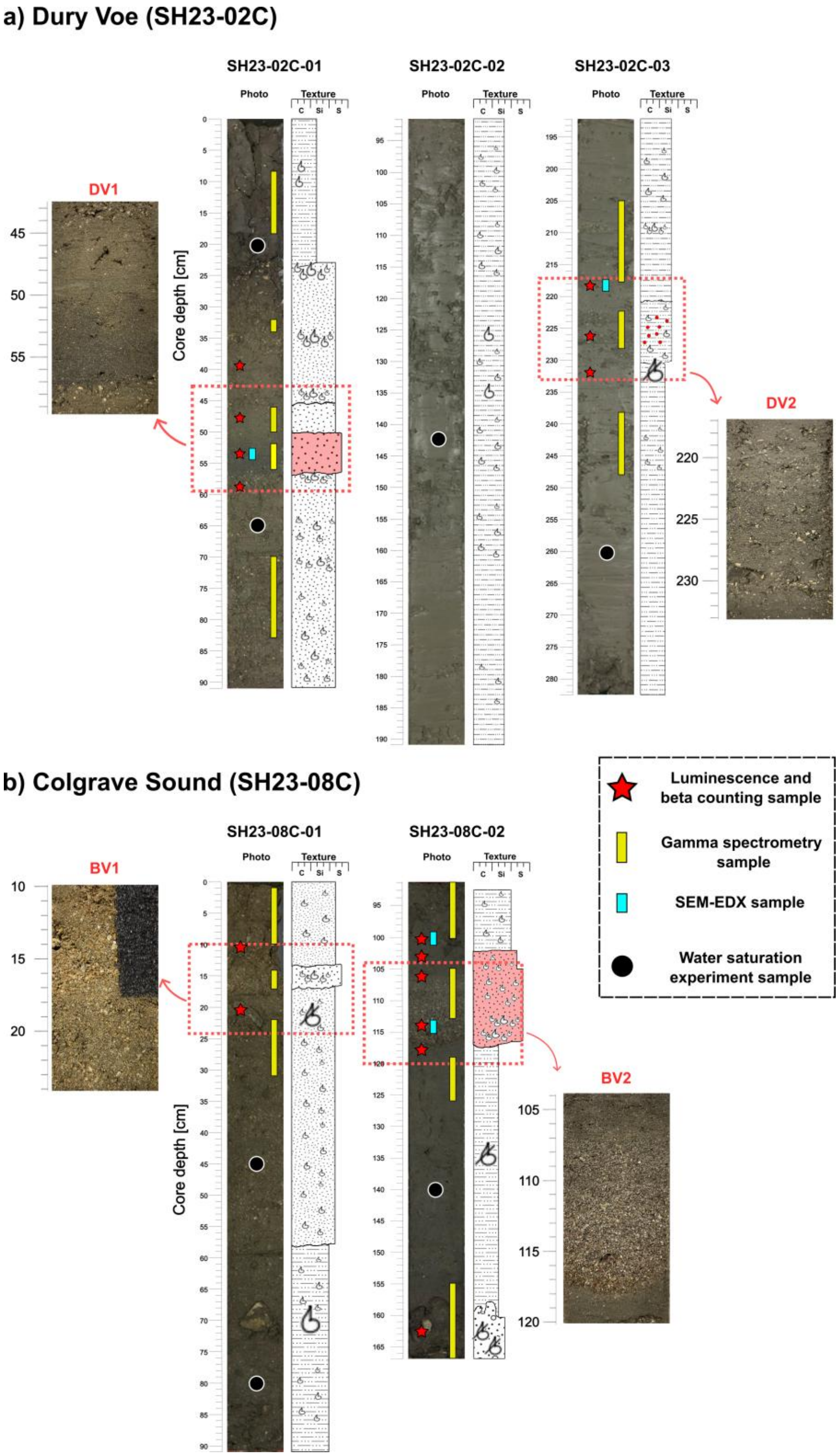

Figure 2: Stratigraphy and sampling scheme of sediment cores a) SH23-02C (Dury Voe) and b) SH23-08C (Colgrave Sound).

https://doi.org/10.5194/egusphere-2026-3279
Preprint. Discussion started: 3 September 2026

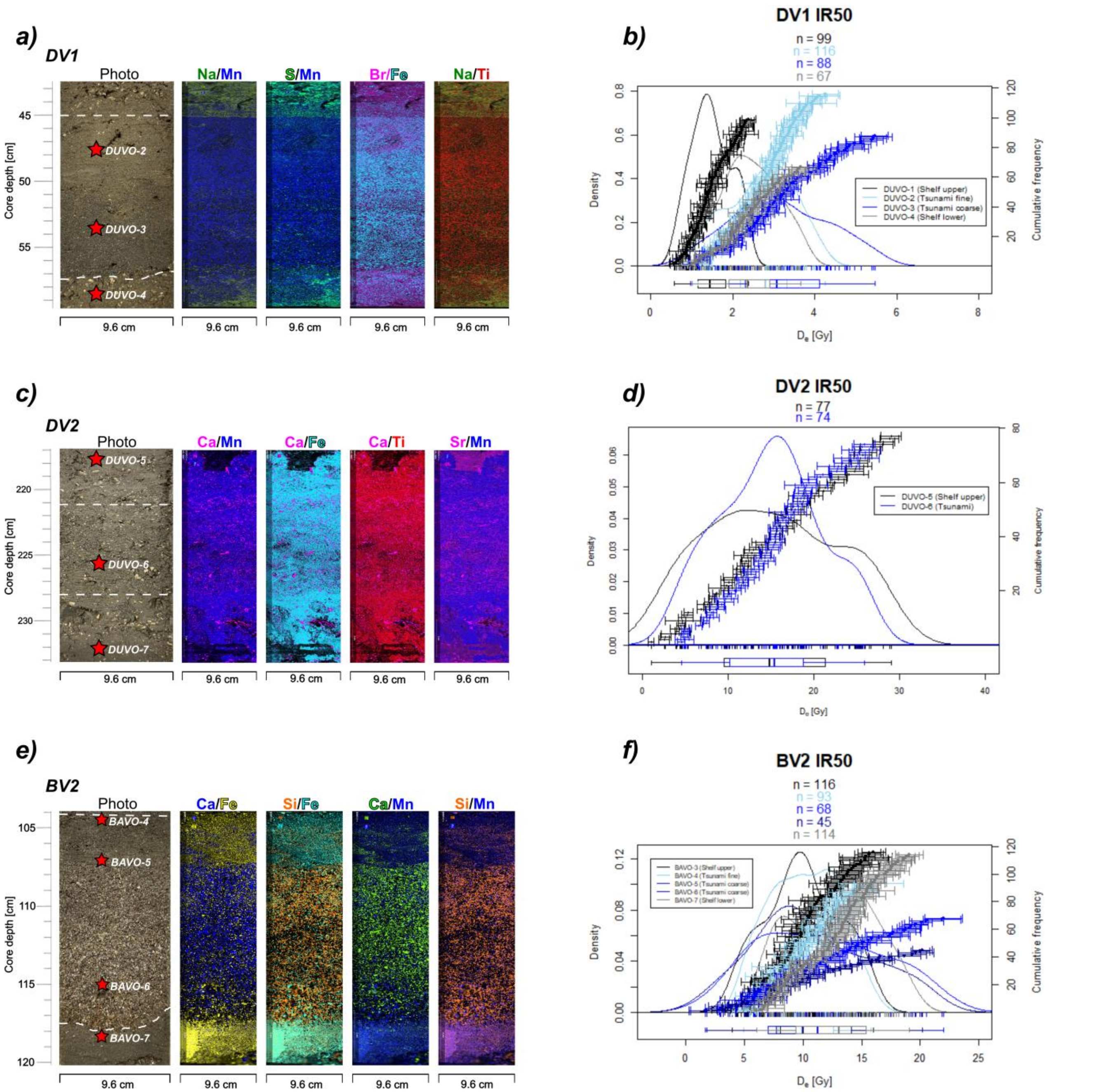

Figure 3: Geometry and D_e distributions of candidate tsunami deposits and background shelf sedimentation. (a, c, e) Optical and µXRF imagery of tsunami deposits and shelf sedimentation found in the Dury Voe (DV1 and DV2) and Colgrave Sound (BV2) core, respectively. Red stars in the optical images indicate position of luminescence samples. White dotted lines indicate layer boundaries. µXRF images contrast two non-quantified, color-coded elements (see heading above each image for respective elements). b, d*, f) KDE plots of SG IR_{50} D_e distributions of luminescence samples from within and surrounding corresponding tsunami deposits. *The D_e distribution of DUVO-7 is not plotted in (d) as only fine-grain measurements exist for this sample.

https://doi.org/10.5194/egusphere-2026-3279
Preprint. Discussion started: 3 September 2026

4.2 Environmental dose rates

Radionuclide contents, measured and saturation water contents, measured internal K contents, and associated environmental dose rates of polymineralic fine- and coarse-grain K-feldspar based on different scenarios of temporal changes in the U decay chain are summarized in Tables S4, S5, S6, S7 and S8 for all samples. Samples from Dury Voe and Colgrave Sound show sample-specific variations between 30–84% and 30–50% in saturation water content, and 6.6–8.7% and 5.1–9.9% in internal K-content, respectively.

For the Dury Voe core, radionuclide contents derived by gamma-ray spectrometry show significant sample-specific variations and a general trend of increasing concentrations with sample depth (Table 1). Moreover, comparing the activity ratios of ^{238}U and ^{226}Ra reveals significant radioactive disequilibria within the U decay chain for most samples, illustrating a time-dependency of dose rates. Here, the extent of disequilibria fundamentally differs with depth, accompanied by differences between *in-situ* background and candidate event deposition (Fig. 4a). The lowermost section of the Dury Voe core shows a near equilibrium state. At a depth between ~60 cm and ~220 cm, where candidate event deposits are absent, a trend of upward-increasing disequilibria is observed. The presence of DV1 coincides with a reintroduction of a near-equilibrium state, followed by a rapid return to disequilibrium conditions above. For the Colgrave Sound core, radionuclide contents derived by gamma-ray spectrometry show a general trend of increasing concentrations with sample depth, too (Table 1). Again, a time-dependency of dose rates through radioactive disequilibria is given when analyzing $^{238}U/^{226}Ra$ ratios (Fig. 4b). However, disequilibria at Colgrave Sound are less significant and there is no obvious pattern between background and candidate event deposits as observed at offshore Dury Voe. The lowermost section of the Colgrave Sound core shows a near-equilibrium state and a more significant disequilibrium is measured up to a depth of ~90 cm. In the uppermost part of the Colgrave Sound core, a near-equilibrium state is detected, with $^{238}U/^{226}Ra$ ratios similar to the lowermost part of the core.

https://doi.org/10.5194/egusphere-2026-3279
Preprint. Discussion started: 3 September 2026

Table 1: Dose rate information for all samples used in this study. DR_{mod} indicate final dose rates used for dating and were modeled under the assumption that ^{230}Th installs disequilibria in the U decay chain. DR_{mod} were eventually calculated using saturation water contents derived from experiments (Table S6) and site-specific K-contents derived from beta counting and SEM-EDX (Table S7).

Luminescence sample	Grain-size fraction [µm]	Signal	U [ppm]	Th [ppm]	K [%]	Saturation water content [%]	Internal K content [%]	DR_{mod} [Gy/ka]
DUVO-1	150–200	IR$_{50}$	1.34 ± 0.09	5.38 ± 0.38	1.33 ± 0.03	62 ± 10	7.0 ± 2.0	1.75 ± 0.16
		pIRIR$_{130}$						1.78 ± 0.16
DUVO-2	200–250	IR$_{50}$	1.59 ± 0.11	6.45 ± 0.46	1.64 ± 0.04	30 ± 10	7.0 ± 2.0	2.34 ± 0.22
		pIRIR$_{130}$						2.37 ± 0.23
	150–200	IR$_{50}$						2.28 ± 0.20
		pIRIR$_{130}$						2.31± 0.26
DUVO-3	200–250	IR$_{50}$	1.55 ± 0.11	5.80 ± 0.42	1.75 ± 0.05	30 ± 10	7.0 ± 2.0	2.39 ± 0.24
		pIRIR$_{130}$						2.41 ± 0.24
DUVO-4	100–150	IR$_{50}$	1.55 ± 0.11	7.02 ± 0.49	1.47 ± 0.04	62 ± 10	7.0 ± 2.0	1.90 ± 0.14
		pIRIR$_{130}$						1.94 ± 0.22
DUVO-5	200–250	IR$_{50}$	2.67 ± 0.18	10.84 ± 0.75	2.32 ± 0.06	66 ± 10	7.0 ± 2.0	2.51 ± 0.23
		pIRIR$_{130}$						2.54 ± 0.23
	150–200	IR$_{50}$						2.45 ± 0.37
		pIRIR$_{130}$						2.49 ± 0.24
DUVO-6	150–200	IR$_{50}$	2.67 ± 0.18	10.84 ± 0.75	2.32 ± 0.06	66 ± 10	7.0 ± 2.0	2.31 ± 0.20
		pIRIR$_{130}$						2.34 ± 0.23
	200–250	IR$_{50}$						2.38 ± 0.20
		pIRIR$_{130}$						2.40 ± 0.20
DUVO-7	4–11	IR$_{50}$	2.67 ± 0.18	10.84 ± 0.75	2.32 ± 0.06	66 ± 10	7.0 ± 2.0	2.78 ± 0.12
		pIRIR$_{130}$						3.07 ± 0.12
BAVO-1	200–250	IR$_{50}$	0.50 ± 0.04	1.81 ± 0.13	0.77 ± 0.02	40 ± 10	5.3 ± 2.0	1.04 ± 0.16
		pIRIR$_{130}$						1.06 ± 0.17
BAVO-2	200–250	IR$_{50}$	0.72 ± 0.05	3.28 ± 0.23	0.89 ± 0.02	50 ± 10	5.3 ± 2.0	1.17 ± 0.15
		pIRIR$_{130}$						1.18 ± 0.19
BAVO-3	150–200	IR$_{50}$	1.17 ± 0.08	4.84 ± 0.34	1.66 ± 0.04	50 ± 10	7.0 ± 2.0	1.82 ± 0.13
		pIRIR$_{130}$						1.84 ± 0.14
	4–11	IR$_{50}$						1.82 ± 0.05
		pIRIR$_{130}$						1.99 ± 0.06
BAVO-4	150–200	IR$_{50}$	0.68 ± 0.05	2.43 ± 0.18	0.93 ± 0.02	30 ± 10	7.0 ± 2.0	1.42 ± 0.12
		pIRIR$_{130}$						1.44 ± 0.14
BAVO-5	200–250	IR$_{50}$	0.68 ± 0.05	2.43 ± 0.18	0.93 ± 0.02	30 ± 10	7.0 ± 2.0	1.49 ± 0.16
		pIRIR$_{130}$						1.50 ± 0.22
BAVO-6	200–250	IR$_{50}$	0.68 ± 0.05	2.43 ± 0.18	0.93 ± 0.02	30 ± 10	7.0 ± 2.0	1.50 ± 0.17
		pIRIR$_{130}$						1.51 ± 0.32
BAVO-7	150–200	IR$_{50}$	1.48 ± 0.10	5.24 ± 0.37	1.37 ± 0.04	50 ± 10	7.0 ± 2.0	1.67 ± 0.13
		pIRIR$_{130}$						1.69 ± 0.16
BAVO-8	200–250	IR$_{50}$	1.38 ± 0.09	5.44 ± 0.38	1.56 ± 0.04	40 ± 10	10.0 ± 2.0	2.21 ± 0.21
		pIRIR$_{130}$						2.22 ± 0.22

https://doi.org/10.5194/egusphere-2026-3279
Preprint. Discussion started: 3 September 2026

The alpha-spectrometry measurements for selected samples (Table S5) demonstrate that disequilibria in the cores are installed at ^{238}U's daughter nuclide ^{230}Th, which is associated with the presence of biogenic carbonates. This finding backs the chosen dose rate modeling approach using three scenarios (i.e., DR_{min}, DR_{max}, DR_{mod}; Table S8). Sensitivity tests of environmental dose rates to these scenarios using saturation water contents and site-specific internal K contents show deviations of DR_{mod} to the endmembers of DR_{min} and DR_{max} in the range of +11.5% and -5.4% which is within the systematic error range of luminescence dating. To account for time-dependent dose rates, environmental dose rates of DR_{mod} (with saturation water contents and site-specific K-contents) are used for all luminescence dating purposes. DR_{mod} show differences between sand (lower values) and finer-grained deposits (higher values), but no clear vertical dose rate trend can be observed in sediments with comparable grain size (Table 1).

We also tested the sensitivity of DR_{mod} for variations of water contents (i.e., saturation versus measured water contents) as well as K contents (i.e., literature values of Smedley et al., 2012, versus site-specific values). In contrast to sensitivities of different radiation field scenarios, dose rates exhibit a high sensitivity against measured gravimetric water contents, showing deviations of up to +43.3% compared to those considering water saturation (Table S9). Using different internal K contents, however, reveals different dose rate sensitivities between our field sites. Dose rates are less sensitive at Dury Voe, where deviations range from 0% to +8.6% and are thus within the systematic error range of luminescence dating. In contrast, dose rates at Colgrave Sound are highly sensitive to changes in internal K content which is illustrated by an increase of up to 29.8% when applying literature values (Table S9). Site-specific discrepancies in sensitivities to internal K content are related to differences in overall radionuclide concentrations: measured internal K contents at Dury Voe overlap within errors with values in Smedley et al. (2012), whereas low radionuclide concentrations at Colgrave Sound would result in significant age underestimations when using these literature values.

https://doi.org/10.5194/egusphere-2026-3279
Preprint. Discussion started: 3 September 2026

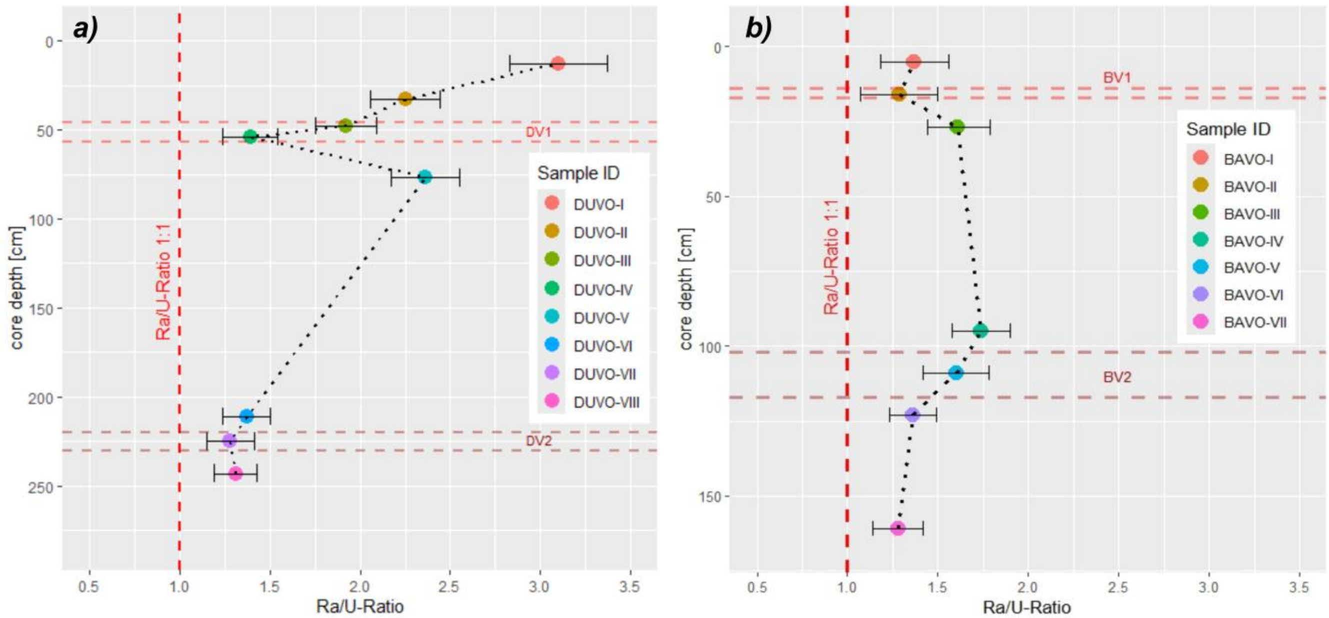

Figure 4: Radioactive disequilibria with core depth at a) Dury Voe and b) Colgrave Sound.

4.3 K-feldspar luminescence properties of offshore samples

The sensitivity of the IR_{50} and $pIRIR_{130}$ luminescence signals is adequate for dating (i.e. the signals exceed three times the background) of both fine and coarse grains (Fig. S1). For luminescence samples from Colgrave Sound, initial tests reveal that a stable background of the pIRIR signal is not reached within a standard stimulation time of 300 s. Therefore, we increase the stimulation time of the pIRIR signal for luminescence samples from Colgrave Sound to 500 s which may point to a more challenging bleaching behavior of the Colgrave Sound samples.

Based on displaying appropriate dose recovery ratios (Figs. S2a and S3a), low residual doses (Figs. S2b, S3b), as well as moderate fading (Figs. S2c, S3c), a $pIRIR_{130}$ protocol with a preheat temperature of 160 °C is chosen for this study (Table S3). Dose recovery tests show adequate reproducibility of laboratory doses with the selected protocols for IR_{50} (ratios between measured and given dose of 0.90–0.99), and $pIRIR_{130}$ (0.87–0.97) after subtraction of laboratory residual doses (Figs. S2d, S3d). Laboratory residual doses of 0.32–0.86 Gy for IR_{50} and 0.33–1.38 Gy for $pIRIR_{130}$ remain below ~5% of the associated paleodoses for all samples except for BAVO-1 and BAVO-2 (Figs. S2e, S3e). Here, residuals may be problematic as values of the IR_{50} signal are even higher than associated paleodoses, and account for more than 70% of the $pIRIR_{130}$ paleodose. Moderate impact of fading on IR_{50} signals is indicated by g-values of 2.3–4.0%/decade, for which corresponding IR_{50} ages of all samples are corrected using site-specific g-values calculated as mean values of fading rates from both coarse-grain (SG, MG) and fine-grain (poly) samples for Dury Voe and Colgrave Sound, respectively (Table 2). For $pIRIR_{130}$ signals, mean g-values of 0.5%/decade indicate minimal impact of fading for Dury Voe, which is why corresponding $pIRIR_{130}$ ages are not corrected (Fig. S2f). Conversely, mean g-values of 1.4 (coarse grain) and 1.9 (FG) %/decade indicate moderate impact of fading on $pIRIR_{130}$ signals at Colgrave Sound, so that corresponding $pIRIR_{130}$ ages are corrected, too (Fig. S3f).

SG doses are normally distributed or right skewed for most samples and signals (Figs. S4, S5) and show overdispersion values of 27–62% for IR_{50}, and 0–44% for $pIRIR_{130}$ (Table S10). The overdispersion of MG aliquots is generally smaller with values of 13–47% for IR_{50} and 9–30% for $pIRIR_{130}$, and 0% for silt-sized polyminerals. The overdispersion of best-bleached sediments from the setting targeted for dating (i.e. σb) is estimated to 31 ± 3% and 13 ± 2% for IR_{50} SG and MG, and 17 ± 4% (Dury Voe) / 20 ± 4% (Colgrave Sound) and 9 ± 2% for $pIRIR_{130}$ SG and MG (Fig. S10). Corresponding σb-values are applied for paleodose calculations using the MAM (for right skewed D_e distributions) and the FMM (for multi-populational D_e distributions).

Diverging patterns appear when comparing SG IR_{50} D_e distributions of luminescence samples from candidate event deposits and their bracketing sediments (Fig. 3b,d,f). In general, background sedimentation shows less broadly scattered distributions than the candidate event deposits. Regarding DV1, sediments above (DUVO-1) are less scattered than below (DUVO-4). Additionally, the finer fraction of DV1 (DUVO-2) is less scattered than its coarser part (DUVO-3). For DV2, sediments above (DUVO-5) and within (DUVO-6) the candidate event deposit show almost identical dose distributions (Fig. 3d). For BV2, background sedimentation once again shows less scattered doses than samples from the candidate event deposit. The coarser section of BV2 (BAVO-5 and BAVO-6) is more scattered than its finer fraction (BAVO-4) which, in turn, shows patterns similar to those of the background sediments (BAVO-3 and BAVO-7).

4.4 Luminescence ages and final chronologies

Table 2 shows a summary of final chronologies based on measured and modeled luminescence ages. Overall, measured luminescence chronologies reveal ages that are in stratigraphic order (i.e., ages increasing with sampling depth). Luminescence samples from the same candidate event deposit exhibit luminescence ages that overlap within errors. In the Colgrave Sound core, notable hiatuses are present both below (BAVO-7) and above (BAVO-3) the lower candidate event deposit (BV2).

Table 2: Summary of information used for final chronologies. *Samples taken directly from candidate tsunami deposits. [†]Luminescence ages that were inserted in the OxCal age-depth models. Fading rates (i.e. g-values) were calculated using t_c values of 429 seconds (IR_{50}) and 726 seconds ($pIRIR_{130}$), respectively. Age_{OxCal} indicate final ages from the OxCal age-depth models. Dose rates of SG and MG measurements vary as different grain-size fractions were measured (Table S8).

Sample	Aliquot size	Signal	Dose model	Paleodose [Gy]	DR_{mod} [Gy/ka]	g-value [%/dec]	Age_{Lumi} [ka]	Age_{Oxcal} [ka]
DUVO-1	SG	IR_{50}	CAM	1.43 ± 0.05	1.75 ± 0.16	2.97 ± 0.52	1.02 ± 0.11[†]	**1.06 ± 0.15**
		$pIRIR_{130}$	CAM	1.98 ± 0.07	1.78 ± 0.16	-	1.11 ± 0.11[†]	
DUVO-2*	SG	IR_{50}	CAM	2.62 ± 0.07	2.34 ± 0.22	2.97 ± 0.52	1.42 ± 0.16[†]	**1.47 ± 0.14**
		$pIRIR_{130}$	CAM	3.41 ± 0.12	2.37 ± 0.23	-	1.44 ± 0.15[†]	
	MG	IR_{50}	CAM	2.67 ± 0.09	2.28 ± 0.20	2.97 ± 0.52	1.48 ± 0.16	
		$pIRIR_{130}$	FMM	3.57 ± 0.29	2.31 ± 0.26	-	1.55 ± 0.21	

https://doi.org/10.5194/egusphere-2026-3279
Preprint. Discussion started: 3 September 2026

DUVO-3*	SG	IR$_{50}$	CAM	2.97 ± 0.13	2.39 ± 0.24	2.97 ± 0.52	1.57 ± 0.19†	
		pIRIR$_{130}$	CAM	3.92 ± 0.15	2.41 ± 0.24	-	1.63 ± 0.17†	
DUVO-4	SG	IR$_{50}$	CAM	2.29 ± 0.09	1.90 ± 0.14	2.97 ± 0.52	1.53 ± 0.15†	**1.55 ± 0.15**
		pIRIR$_{130}$	FMM	2.61 ± 0.25	1.94 ± 0.22	-	1.35 ± 0.20†	
DUVO-5	SG	IR$_{50}$	FMM	17.35 ± 0.87	2.51 ± 0.23	2.97 ± 0.52	8.99 ± 1.09†	**8.11 ± 0.50**
		pIRIR$_{130}$	CAM	22.96 ± 1.00	2.54 ± 0.23	-	9.04 ± 0.91†	
	MG	IR$_{50}$	MAM	16.47 ± 2.18	2.45 ± 0.37	2.97 ± 0.52	8.74 ± 1.87	
		pIRIR$_{130}$	MAM	24.17 ± 1.62	2.49 ± 0.24	-	9.71 ± 1.14	
DUVO-6*	SG	IR$_{50}$	FMM	16.20 ± 0.80	2.31 ± 0.20	2.97 ± 0.52	9.12 ± 1.08†	**8.69 ± 0.37**
		pIRIR$_{130}$	CAM	19.10 ± 1.31	2.34 ± 0.23	-	8.16 ± 0.98†	
	MG	IR$_{50}$	CAM	17.47 ± 0.54	2.38 ± 0.20	2.97 ± 0.52	9.56 ± 1.03	
		pIRIR$_{130}$	CAM	26.11 ± 0.64	2.40 ± 0.20	-	10.88 ± 0.95	
DUVO-7	Poly	IR$_{50}$	CAM	16.91 ± 0.12	2.78 ± 0.12	4.04 ± 0.52	8.83 ± 0.69†	**8.86 ± 0.35**
		pIRIR$_{130}$	CAM	26.78 ± 0.27	3.07 ± 0.12	-	8.72 ± 0.35†	
BAVO-1	SG	IR$_{50}$	CAM	0.28 ± 0.02	1.04 ± 0.16	3.13 ± 0.40	0.34 ± 0.05†	**0.33 ± 0.13**
		pIRIR$_{130}$	FMM	1.03 ± 0.10	1.06 ± 0.17	1.43 ± 0.50	1.08 ± 0.21	
BAVO-2	SG	IR$_{50}$	CAM	0.53 ± 0.03	1.17 ± 0.15	3.13 ± 0.40	0.57 ± 0.08†	**0.61 ± 0.15**
		pIRIR$_{130}$	FMM	1.15 ± 0.13	1.18 ± 0.19	1.43 ± 0.50	1.08 ± 0.22	
BAVO-3	SG	IR$_{50}$	CAM	9.66 ± 0.29	1.82 ± 0.13	3.13 ± 0.40	6.98 ± 0.64†	**6.95 ± 0.69**
		pIRIR$_{130}$	CAM	15.15 ± 0.63	1.84 ± 0.14	1.43 ± 0.50	9.28 ± 0.92	
	Poly	IR$_{50}$	CAM	13.02 ± 0.09	1.82 ± 0.05	3.82 ± 0.18	10.20 ± 0.36	
		pIRIR$_{130}$	CAM	24.00 ± 0.27	1.99 ± 0.06	1.86 ± 1.47	14.20 ± 2.33	
BAVO-4*	SG	IR$_{50}$	CAM	9.86 ± 0.30	1.42 ± 0.12	3.13 ± 0.40	9.17 ± 0.95†	**8.75 ± 0.63**
		pIRIR$_{130}$	CAM	12.18 ± 0.76	1.44 ± 0.14	1.43 ± 0.50	9.54 ± 1.20	
BAVO-5*	SG	IR$_{50}$	CAM	10.74 ± 0.62	1.49 ± 0.16	3.13 ± 0.40	9.53 ± 1.26†	
		pIRIR$_{130}$	FMM	11.53 ± 1.28	1.50 ± 0.22	1.43 ± 0.50	8.66 ± 1.66	
BAVO-6*	SG	IR$_{50}$	CAM	10.10 ± 0.68	1.50 ± 0.17	3.13 ± 0.40	8.89 ± 1.27†	
		pIRIR$_{130}$	MAM	15.57 ± 2.93	1.51 ± 0.32	1.43 ± 0.50	11.64 ± 3.37	
BAVO-7	SG	IR$_{50}$	CAM	12.18 ± 0.34	1.67 ± 0.13	3.13 ± 0.40	9.64 ± 0.91†	**10.09 ± 0.72**
		pIRIR$_{130}$	CAM	15.33 ± 0.91	1.69 ± 0.16	1.43 ± 0.50	10.23 ± 1.23	
BAVO-8	SG	IR$_{50}$	CAM	18.00 ± 0.64	2.21 ± 0.21	3.13 ± 0.40	10.79 ± 1.20†	**11.07 ± 0.93**
		pIRIR$_{130}$	CAM	23.22 ± 1.12	2.22 ± 0.22	1.43 ± 0.50	11.81 ± 1.41	

The relative dating accuracy of the luminescence ages can be evaluated between different aliquot sizes (SG, MG) and luminescence signals (IR$_{50}$, pIRIR$_{130}$). MG ages from both sites tend to show older ages than their SG counterparts (Fig. 5a). When comparing them to ages of known tsunami events in the Shetlands, it seems that MG ages, and especially those of the

https://doi.org/10.5194/egusphere-2026-3279
Preprint. Discussion started: 3 September 2026

pIRIR$_{130}$ signal, overestimate the true burial age. This finding is supported by the fact that overdispersion values, as potential indicators of incomplete bleaching for a portion of grains, of corresponding SG measurements are comparatively high (Fig. S10). Thus, age overestimations of MG measurements may result from averaging effects of higher D_e values of incompletely bleached grains that cannot be isolated by means of MG aliquots. Therefore, we decide to exclude all coarse-grained MG ages for Bayesian age-depth modeling, and thus, for interpreting final chronologies. We note that the age assessment of one sample (DUVO-7) solely relies on MG measurements using polymineralic fine-grained sediment. Although it is not possible to ultimately assess performance for silt-sized deposits, corresponding luminescence ages of DUVO-7 are implemented in age-depth modeling because they appear reasonable in stratigraphic context (Table 2).

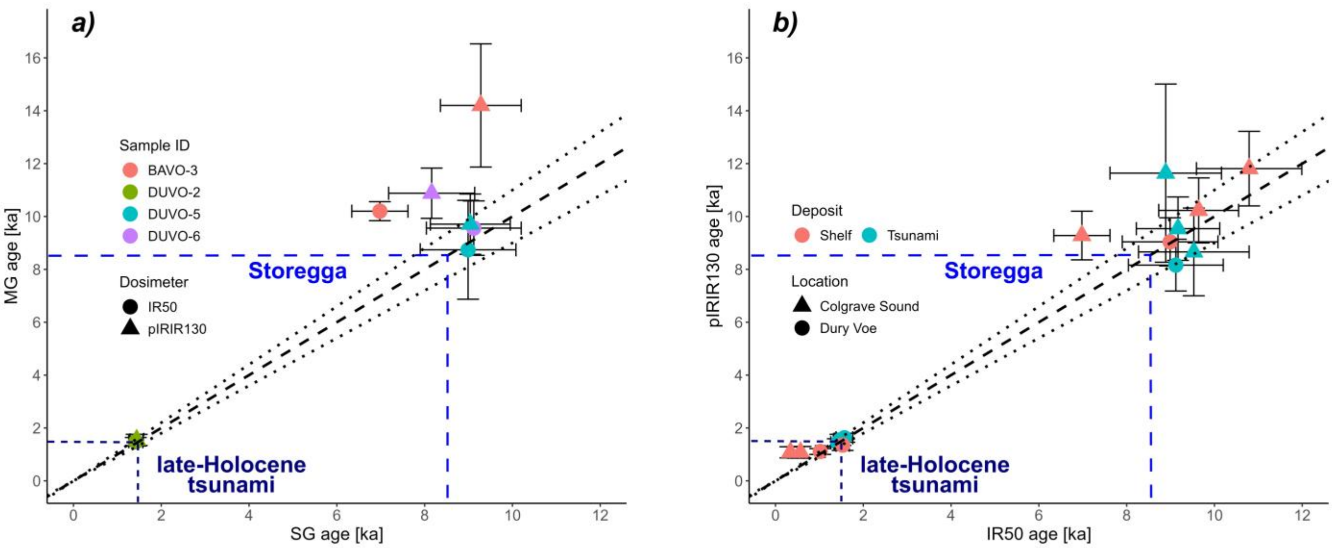

Figure 5: Evaluation of luminescence ages in the absence of independent age control. a) SG vs MG ages for both IR$_{50}$ and pIRIR$_{130}$ signals. b) IR$_{50}$ vs pIRIR$_{130}$ for SG ages of candidate tsunami and shelf deposits. Dotted lines indicate 1:1 ± 10% ratio.

When comparing IR$_{50}$ and pIRIR$_{130}$ ages of SG measurements, the linear regression plot in Figure 5b reveals an overall good performance of both signals with a tendency of pIRIR$_{130}$ showing older ages than IR$_{50}$ ages. Again, when comparing IR$_{50}$ and pIRIR$_{130}$ ages of samples taken from candidate event deposits to ages of known tsunami events, pIRIR$_{130}$ ages, especially from Colgrave Sound, seem to overestimate the true burial age. Figure 5b also demonstrates that age discrepancies between IR$_{50}$ and pIRIR$_{130}$ ages are more pronounced for shelf sediments than for candidate event deposits. We therefore decide to exclude SG ages of pIRIR$_{130}$ signals for Bayesian age-depth modeling of the Colgrave Sound core but include both SG ages from IR$_{50}$ and pIRIR$_{130}$ signals for age-depth modeling of the Dury Voe core. Another aspect supporting the exclusion of pIRIR$_{130}$ ages for Colgrave Sound is given by the observed luminescence properties. As previously stated, due to insufficient signal resetting, illumination time of the Colgrave Sound pIRIR$_{130}$ signal was increased from 300 s to 500 s. This indicates that K-feldspar originating from Colgrave Sound may exhibit poorer signal resetting than K-feldspar from Dury Voe.

https://doi.org/10.5194/egusphere-2026-3279
Preprint. Discussion started: 3 September 2026

The K-feldspar luminescence ages are further used to refine the overall core chronologies, and especially to improve the dating accuracy of candidate event deposits, by Bayesian age-depth modeling in OxCal (Fig. 6). For candidate event deposits preserved in the Dury Voe core, OxCal chronologies yield ages of 1.47 ± 0.14 ka for DV1, and 8.69 ± 0.37 ka for DV2 (Fig. 6a). For candidate event deposits preserved in the Colgrave Sound core, OxCal chronologies yield ages of 0.52 ± 0.17 ka for BV1, and 8.75 ± 0.63 ka for BV2 (Fig. 6b).

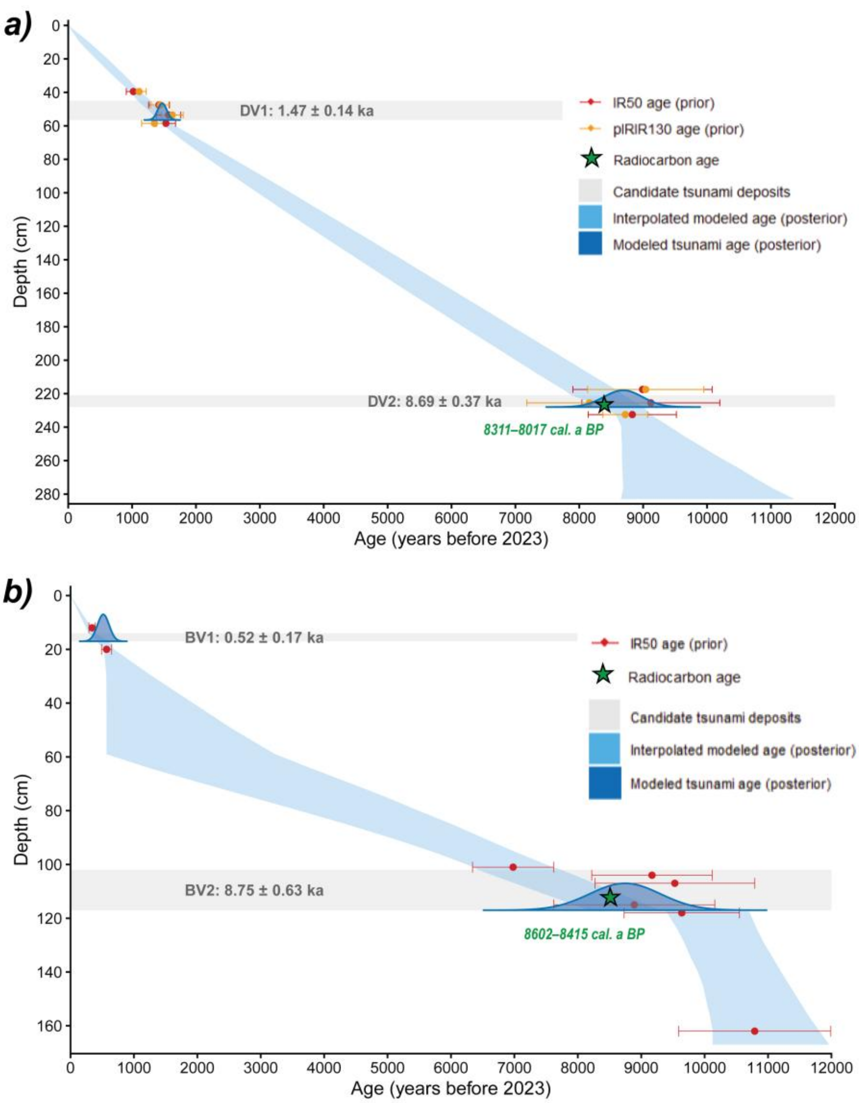

Figure 6: Age-depth models of cores a) SH23-02C (Dury Voe) and b) SH23-08C (Colgrave Sound) based on K-feldspar luminescence ages. For SH23-02C (a) both IR_{50} (red) and $pIRIR_{130}$ (orange) SG ages were inserted as priors to the model; for SH23-08C (b) only IR_{50} (red) SG ages were inserted as priors to the model. Blue bell curves indicate modeled ages of respective candidate tsunami deposits. Blue ribbons indicate the interpolated age-depth model based on the outputs of OxCal P-sequence models. Green asterisks show radiocarbon ages of shell samples from parallel/proximal cores in An Nahar et al. (under review).

https://doi.org/10.5194/egusphere-2026-3279
Preprint. Discussion started: 3 September 2026

5 Discussion

5.1 Interpretation of event deposits preserved at offshore Dury Voe and Colgrave Sound

Both cores of this study show overall good correlation with their parallel cores and with the basin-wide stratigraphy as discussed by An Nahar et al. (under review). All three event deposits identified by An Nahar et al. (under review) are stratigraphically congruent with the candidate event deposits from this study.

At Dury Voe, high-amplitude seismic intervals, HAI1 and HAI2, that were identified on high-resolution seismic data (An Nahar et al., under review) correlate with candidate event deposits DV2 and DV1 (this study), respectively. An Nahar et al. (under review) describe both units as normally graded, poorly sorted coarse sand layers with abundant, generally angular shell fragments, interbedded in shallow-marine background sedimentation. They find that HAI1 (correlated to DV2 in this study) exhibits a slightly coarser-grained texture than HAI2 (correlated to DV1 in this study). Their parallel core shows slightly different sedimentological patterns. Whereas DV1 reveals similar sedimentological characteristics as HAI2, DV2 is barely identifiable by the naked eye (Fig. 2) but upper and lower boundaries can be detected by µXRF. This underpins the importance of collecting multiple cores, even in the same coring location, and further demonstrates the effectiveness of µXRF mapping to identify the nature of depositional boundaries of event deposits in the offshore realm. Elemental mapping shows that DV2 is a deposit with slightly higher carbonate content compared to its surrounding terrestrial-influenced background sedimentation (Fig. 3c). Interestingly, µXRF mapping of DV1 reveals reversed compositional patterns compared to DV2, because here, the event deposit shows as a terrestrial-dominated unit interbedded in marine background sedimentation (Fig. 3a). This suggests that the two event deposits at offshore Dury Voe are interbedded in different facies, possibly associated with the postglacial RSL history and sedimentary evolution (An Nahar et al., under review; Earland et al., 2024). Final chronologies presented in this study date DV2 to 8.69 ± 0.37 ka. This luminescence-based age is in accordance with a shell-derived radiocarbon age of 8311–8017 cal. a BP from a parallel core (Fig. 6a; An Nahar et al. under review). Thus, based on the sedimentological, geochemical, and geochronological data, DV2 can be identified as a Storegga tsunami deposit. DV1 dates to 1.47 ± 0.14 ka and there is no direct age control from radiocarbon dating for this unit from a parallel core. However, in combination with sedimentological and geochemical data presented above, DV1 can be linked to the 1400 cal. a BP tsunami.

At Colgrave Sound, candidate event deposit BV2 (this study) correlates with seismic-stratigraphic unit CB-SU3 in An Nahar et al. (under review). CB-SU3 is described as a normally graded sandy deposit with a sharp basal contact, poor sorting, and abundant angular shell fragments, which perfectly aligns with observations of BV2. µXRF mapping further ascribes the event deposit to a potentially marine-sourced deposit embedded in terrestrial-dominated background sedimentation (Fig. 3e). A radiocarbon age of a shell sample that was taken from the event deposit from a close-by site (SH23-07) yielded an age of 8602–8415 cal. a BP (An Nahar et al., under review) which overlaps with the luminescence-based age estimate of 8.75 ± 0.63 ka for BV2 establishing an unequivocal link to the Storegga tsunami. Additionally, in this study, we exclusively describe another candidate event deposit, BV1, interbedded in the uppermost facies unit of the Colgrave Sound core. An Nahar et al. (under review) describe this uppermost facies unit to consist of bioclastic medium- to coarse-grained sand with localized

https://doi.org/10.5194/egusphere-2026-3279
Preprint. Discussion started: 3 September 2026

coarser pockets of shell hash. It is therefore possible that BV1 represents one of these coarser-grained pockets. The luminescence-based chronology dates BV1 to 0.52 ± 0.17 ka years, much younger than the late-Holocene tsunami, which is preserved in onshore sediment records at nearby Basta Voe (Dawson et al., 2006). The origin of BV1 remains open, as it may be the result of a very local submarine slump induced by an extreme storm given the frequent phases of high storminess over the last 1500 years (Hess et al., 2024), or a local sub-facies related to variations in location and/or intensity of bottom currents (An Nahar et al., under review).

5.2 Potential of the Shetland's offshore sedimentary record for studying tsunami deposits

This study identifies three tsunami deposits preserved in offshore sedimentary records from two embayments of the Shetland Islands. Tsunami deposits of the Storegga tsunami are found at both offshore Colgrave Sound/Basta Voe and Dury Voe, and in addition, sedimentary evidence of the late-Holocene tsunami is found in the offshore record of Dury Voe. While this does not extend the regional tsunami catalog for the North Sea region, findings of this study demonstrate the huge potential of utilizing offshore records for reconstructing tsunami events and establishing long-term tsunami chronologies (An Nahar et al., under review; Earland et al., 2024; Feist et al., 2023; Schwarzer, 2020).

The Storegga event was previously identified offshore in the deep Fetlar Basin (Earland et al., 2024) and was recently traced into shallower marine settings including Dury Voe and Basta Voe (An Nahar et al., under review), as confirmed by this study. In the absence of onshore evidence, the presence of Storegga tsunami deposits at offshore Dury Voe and Colgrave Sound demonstrates the potential of the Shetland's offshore record to extend the local tsunami catalog. However, Colgrave Sound's/Basta Voe's offshore record does not reveal evidence of the late-Holocene tsunami (An Nahar et al., under review) which is well-preserved onshore at Basta Voe (Dawson et al., 2006). Storegga tsunami deposits closest to Dury Voe were identified in the coastal lake records of Loch of Benston and Garth Loch, south of Dury Voe near Cat Firth. These two lakes also represent the exclusive sites of the mid-Holocene tsunami (Bondevik et al., 2005). The offshore core from Dury Voe does not exhibit sedimentary evidence or traces of such an event, and thus, fuels the debate of its existence (Long, 2015). Revisiting and dating the so far only radiocarbon-dated lake deposits from Garth Loch and Loch of Benston by means of luminescence may help to establish independent age control of the mid-Holocene tsunami, and to support or question a tsunamigenic origin.

The preservation of the late-Holocene tsunami at offshore Dury Voe, which was also found in its onshore records (Bondevik et al., 2005; Nussberger et al., under review), proves that onshore and offshore tsunami deposits from the Shetlands can be coupled.

The Storegga tsunami deposits differ considerably in their depositional signature. While it is exceptionally preserved at Colgrave Sound, its counterpart at Dury Voe appears more cryptic and disturbed. These differences may go back to varying preservation potentials conditioned by Holocene RSL. At the time of the Storegga tsunami, RSL in the North Sea is projected ~34–27 m lower than today (e.g., An Nahar et al., under review; Bradley et al., 2023; Dawson et al., 2020; Shennan et al., 2018), leaving the coring site at Colgrave Sound (81 m present-day water depth) under calm conditions below the storm wave

https://doi.org/10.5194/egusphere-2026-3279
Preprint. Discussion started: 3 September 2026

base at that time. In contrast, the site at Dury Voe (36 m present-day water depth) was a highly dynamic, very shallow-marine environment which may have resulted in post-depositional alteration of the Storegga tsunami deposit.

Although it is not possible to directly compare the elemental ratios of identified tsunami deposits (Fig. 3 a,c,e), underlying µXRF imagery may offer insights into tsunami transport mechanisms (i.e., backwash vs. runup; Costa et al., 2021b; Feist et al., 2023). The poorly preserved Storegga tsunami deposit at Dury Voe shows indications of slightly increased marine influx (i.e. Ca and Sr). In combination with projected RSL, this pattern strengthens the interpretation that Dury Voe's Storegga tsunami deposit is predominantly runup-dominated introducing fully marine sediment into a marginal-marine setting. In contrast, the well preserved Storegga tsunami deposit at Colgrave Sound shows a mixed signal of terrestrial (i.e., Si) and carbonate-rich (i.e., Ca) material which may point to a backwash-dominated deposit mostly sourced from intertidal and nearshore environments.

The exceptional preservation of the late-Holocene tsunami at offshore Dury Voe may be related to a relatively stable RSL over the late Holocene (e.g., Bradley et al., 2023; Dawson et al., 2020; Shennan et al., 2018). A rapidly rising RSL in the early to mid-Holocene may have submerged the Dury Voe location below the storm-wave base, which, in turn, may have led to a much better preservation potential for event deposits in the late Holocene. Underlying µXRF imagery of the deposit shows indications of terrestrial influx (i.e., Fe and Ti), possibly reflecting a backwash component. Since the late-Holocene tsunami was found to be a much smaller-scale event than the Storegga tsunami (Bondevik et al., 2005; Dawson et al., 2006), the presence of a corresponding deposit points out that localized tsunamis can also generate strong channelized backwash (Schwarzer, 2020).

5.3 Accuracy of K-feldspar chronologies for offshore tsunami deposits

Tsunami deposits in offshore sediment cores can be dated with K-feldspar luminescence by targeting both the tsunami layers themselves (direct event ages) and/or the deposits bracketing the event. Nonetheless, this study reveals multiple challenges for luminescence dating offshore tsunami deposits from the Shetland Islands and in general.

Besides complexities related to the luminescence signal itself, inaccuracies of luminescence ages in offshore environments may be caused by challenges related to the robust assessment of environmental dose rates due to long-lived insoluble isotopes and authigenic U (Cunningham et al., 2019), often associated with the presence of biogenic carbonates. Complex radiation fields with radioactive disequilibria in the U decay chain were detected by gamma-ray spectrometry. We assume the presence of calcareous sediments at our field sites to create disequilibria which require the consideration of time-dependent dose rates. Alpha spectrometry measurements allow to determine ^{230}Th as the radioisotope in the U-series that installs the disequilibrium. Although disequilibria are found to be more pronounced at Dury Voe (Fig. 4), sensitivities at both field sites are found to be within the systematic error range of luminescence dating, which is in line with the findings of previous studies (Cunningham et al., 2019; Murray et al., 2021). Nevertheless, we suggest that whenever radioactive disequilibria are present, sensitivities of resulting dose rates should be assessed through modeling approaches (Nentwig et al., 2015; Zander et al., 2007) to achieve robust and accurate environmental dose rates for luminescence chronologies.

The sensitivities of modeled dose rates were further tested for varying water and internal K contents. In our study, both parameters are found to be more significant for the corresponding dose rates than observed radioactive disequilibria. We show that saturation water contents achieved through straightforward laboratory experiments are more suitable for dose rate assessment in offshore settings, as gravimetrically measured water contents are likely underestimating moisture contents due to loss of water during subsampling. The influence of internal K contents on environmental dose rates reveals different results for Dury Voe and Colgrave Sound. Due to generally high radionuclide concentrations, sensitivities of varying internal K contents are comparatively small for samples from Dury Voe. In contrast, internal K contents show as highly sensitive for dose rate assessment at Colgrave Sound where smaller radionuclide concentrations are present. Therefore, we suggest that site- and/or sample-specific internal K contents should be determined when applying K-feldspar luminescence dating in radiation fields with low radionuclide concentrations. Our findings are supported by Maßon et al. (2025) who highlight the potential impact of internal K content on environmental dose rates and luminescence chronologies.

Heterogenous K-feldspar signal resetting has been associated with the presence of right-skewed and largely scattered D_e distributions (López et al., 2018). In our study, systematic shifts are observed for D_e distributions of both IR_{50} and $pIRIR_{130}$ signals as well as between SG and MG measurements (Fig. S4, S5). The rightward shifting of dose distributions based on the $pIRIR_{130}$ signal can be explained through stronger fading of the IR_{50} signal. Fading corrections lead to congruent ages when using the same dose models. The rightward shifting of dose distributions based on MG measurements, however, hints to averaging effects resulting from the presence of older grain populations on aliquots and, thus, a systematic overestimation of the MG-derived ages. Age overestimations of MG measurements have been previously reported for both onshore and offshore tsunami deposits, where they are related to incomplete bleaching as a consequence of turbulent sediment transport and sediment sources with incomplete pre-bleaching (Brill and Tamura, 2020; Brill et al., 2024; Murari et al., 2007). The degree of signal resetting prior to burial can be assessed through comparing the ages of different minerals or different grain sizes and aliquot sizes of the same mineral (Chamberlain et al., 2017; Godfrey-Smith et al., 1988). As quartz is not targeted in this study, the bleaching properties between quartz and feldspar cannot be evaluated. However, age discrepancies between SG and MG measurements have also been used to investigate incomplete bleaching for both onshore (Murari et al., 2007) and offshore tsunami deposits (Brill et al., 2024). When comparing luminescence chronologies of the Storegga tsunami deposit at Dury Voe, SG measurements show ages close to the timing of known tsunami events and the existing radiocarbon chronologies, whereas MG measurements reveal older ages (Fig. 5a). At Dury Voe, where both SG and MG measurements (DUVO-2, 5, and 6) were conducted, K-feldspars show overall good bleaching characteristics as age discrepancies are low (Fig. 5a, Table 2). For Colgrave Sound, bleaching characteristics can only be assessed for MG and SG ages in one shelf sample (BAVO-3) (Fig. 5a). Here, fading-corrected ages show large discrepancies of >3 ka (Table 2). This further supports our hypothesis that incomplete bleaching may be more significant at Colgrave Sound, potentially because of deeper water compared to Dury Voe. Overall, this underlines the importance and necessity of SG measurements, which is recommended by the majority of tsunami-related luminescence studies (e.g., Bateman et al., 2022; Brill et al., 2018; Riedesel et al., 2018) and also confirmed by Brill et al. (2024) for dating offshore tsunami deposits. As most luminescence ages of tsunami deposits in our study rely solely on SG

https://doi.org/10.5194/egusphere-2026-3279
Preprint. Discussion started: 3 September 2026

measurements, an ultimate assessment of bleaching behavior is, however, not permitted. Nevertheless, SG measurements in combination with applying appropriate dose models (i.e., MAM or FMM) allow to isolate populations of potentially incompletely bleached grains from properly bleached grains.

Erosional hiatuses are common in sediment cores preserving offshore tsunami deposits (Brill et al., 2024; Goodman-Tchernov et al., 2009; Reinhardt et al., 2006; Schwarzer, 2020). At Dury Voe, only minor age offsets exist between the bases of tsunami layers and their underlying shelf sediments. At Colgrave Sound, age-depth models indicate erosional hiatuses of >1000 a both below and above the Storegga tsunami deposit. We interpret this as a result of strong erosion during the tsunami and changes in sedimentation rates following the event, and/or more problematic bleaching characteristics in deeper waters. Previous studies have demonstrated that tsunamis can transport most of the sediment volume available in the coastal accommodation space (Spiske, 2020). Thus, the Storegga tsunami may have eroded and transported much of the available sediment in the bay of Basta Voe, triggering extremely low sedimentation rates in deeper waters of its basin following the event. When comparing the age discrepancies between Storegga tsunami deposits from both field sites, it becomes evident that erosion during the Storegga tsunami was much stronger at Colgrave Sound/Basta Voe than at Dury Voe. This underlines the importance of the geomorphic setting and bathymetry for the formation of an offshore tsunami deposit (Schwarzer, 2020).

By accounting for stratigraphic succession and hiatuses, as well as by discriminating between instantaneous and continuous sedimentation, the application of Bayesian modeling significantly improves the accuracy of dating the tsunami deposits in this study. Although K-feldspar luminescence ages are already accurate, age-depth modeling can further reduce error ranges.

5.4 Implications of luminescence analyses for characterizing offshore tsunami deposits

We have shown that the D_e distributions of luminescence samples that were subsampled in a high stratigraphic resolution may help to discriminate transport modes. D_e distributions from the disturbed Storegga tsunami deposit (DV2) and its background shelf sedimentation at offshore Dury Voe are almost identical, pointing to either mixing of tsunami and shelf sediments or overall similar sediment sources. The other two well preserved, coarse and normally graded tsunami deposits (DV1 and BV2) show overlapping patterns of wide D_e distributions which systematically differ from the narrow D_e distributions of the finer background sediments. We therefore hypothesize that these patterns may relate to either different source areas of fine and coarse sediments, and/or different tsunami transport modes with coarser material being transported as bedload (poorer bleaching) and finer material being transported by suspension (better bleaching). Hence, luminescence data may also provide an innovative method to discriminate tsunami and shelf sedimentation as well as different tsunami transport modes (Sugawara, 2020). However, more systematic research is needed to further test this hypothesis.

Distinct patterns regarding the distribution of radioactive disequilibria involves an upward increase at Dury Voe (Fig. 4a), which may be interpreted as increasing marine influence following RSL rise. This interpretation is supported by Nussberger et al. (under review) who found radionuclide activities of the onshore tsunami deposit at Dury Voe to be in equilibrium. The extent of radioactive disequilibria offshore may further respond to the presence of tsunamis, as event deposits coincide with lowest disequilibria at near-equilibrium state. There are two possible explanations for this pattern. Firstly, tsunamis may episodically deposit high sediment loads influencing the balance of radiation fields (Cunningham et al., 2019). Secondly, tsunamis are able to entrain and deposit sediments from various source areas and environments (Spiske, 2020) with different radiation fields. However, radioactive disequilibria at Colgrave Sound were less significant and did not reveal a certain response to event deposits. Thus, these differences may also be conditioned by site-specific geological factors around the Shetland Islands.

6 Conclusions

We presented the first luminescence-based chronology for offshore tsunami deposits from the Shetland Islands, UK. K-feldspar luminescence dating on two offshore sediment cores from the Shetland Islands proved to be an applicable and suitable technique to date both offshore tsunami deposits and shelf sediments. A total of four candidate tsunami deposits were visually identified in the two cores, and three of these were successfully correlated to the wider regional stratigraphic framework (An Nahar et al., under review), while the fourth remained elusive. µXRF mapping proved to be a powerful tool for a rapid and effective assessment of the internal architecture and nature of boundaries of candidate tsunami deposits as well as for refining the sampling strategy for luminescence dating. Complex radiation fields and time-dependency of environmental dose rates in our cores were tackled by a thorough assessment, including the implementation of (1) representative water contents, (2) site-specific internal K contents, and (3) modeled dose rates considering the effect of radioactive disequilibria. Robust luminescence-based chronologies were achieved through measuring silt- and sand-sized K-feldspars with a $pIRIR_{130}$ protocol in combination with Bayesian age-depth modeling.

Our final chronologies indicated sedimentary evidence of the 8150 cal. a BP Storegga tsunami at offshore Dury Voe and Colgrave Sound, and additionally of the 1400 cal. a BP late-Holocene tsunami at offshore Dury Voe. While this did not extend the tsunami catalog for the North Sea region, our findings added to understanding the spatial distribution of local tsunami events and their deposits on the Shetlands. We also showed that our multi-method luminescence dating approach may further improve the characterization of offshore tsunami deposits by discriminating between different transport modes and mechanisms. Overall, our study demonstrated both the potential of luminescence dating for offshore tsunami deposits and the benefits of the associated chronologies for tsunami hazard assessment.

https://doi.org/10.5194/egusphere-2026-3279
Preprint. Discussion started: 3 September 2026

Data availability

The raw data used in this study can be accessed via Zenodo at https://doi.org/10.5281/zenodo.21363495 (Peffeköver et al., 2026).

Author contributions

AP: conceptualization, data curation, formal analysis, investigation (sample collection & laboratory), methodology, visualization, writing (original draft preparation).

ME: conceptualization, investigation (sample collection), methodology, supervision, writing (original draft preparation).

SO: investigation (laboratory), methodology, resources, writing (review and editing)

AZ: investigation (laboratory), methodology, writing (review and editing)

MVD: investigation (sample collection), project administration, writing (review and editing)

PJMC: investigation (sample collection), project administration, writing (review and editing)

SD: writing (review and editing)

RNFAN: investigation (sample collection), writing (review and editing)

JS: writing (review and editing)

VMAH: funding acquisition, project administration, writing (review and editing)

MDB: funding acquisition, project administration, writing (review and editing)

DB: conceptualization, investigation (laboratory), methodology, supervision, resources, writing (original draft preparation).

Competing interests

The authors declare that they have no conflict of interest.

Acknowledgements

We would like to thank all scientific crew members of the RV Belgica Cruise 2023/16: Kamill Lisson, Ruben Bertels, Thomas Goovaerts, Bruno Meyvis, Mariana Teixeira, Francisco Dourado, Henrique Cavadas, Katharina Hess, Jan Vermaut, Wouter Blomme, Yan Weber Mesquita, Camila Stempels Bautista. We further thank all operational and technical crew members of RV Belgica Cruise 2023/16 for enabling smooth operations. We would also like to express our gratitude towards Kathrin Jung and Hanna Cieszynski for helping with preparation for and conducting SEM-EDX measurements. We would like to thank Florian Steininger and Marie Gröbner for their technical support. Andreas Peffeköver would like to thank Erik Strub for discussing radioactive disequlibria.

https://doi.org/10.5194/egusphere-2026-3279
Preprint. Discussion started: 3 September 2026

Financial support

This study is part of the NORSEAT project ("Storegga and beyond – NORth SEA Tsunami deposits offshore Shetland Islands") funded by the Belgian Science Policy Office BELSPO (RV/21/NORSEAT). In-kind contributions were kindly provided by the Cologne Luminescence Laboratory and the Physical Geography Laboratory at University of Cologne.

https://doi.org/10.5194/egusphere-2026-3279
Preprint. Discussion started: 3 September 2026

References

An Nahar, R. N. F., Van Daele, M., Costa, P. J. M., Engel, M., Dawson, S., Scheder, J., Goovaerts, T., Heyvaert, V .M. A., and De Batist, M.: Post-glacial sedimentary evolution and stratigraphy of the shallow offshore areas of the Shetland Islands, EarthArXiv, https://doi.org/10.31223/X53201, under review.

Auclair, M., Lamothe, M., and Huot, S.: Measurement of anomalous fading for feldspar IRSL using SAR, Radiat. Meas., 37, 487–492, https://doi.org/10.1016/S1350-4487(03)00018-0, 2003.

Batchelor, C. L., Margold, M., Krapp, M., Murton, D. K., Dalton, A. S., Gibbard, P. L., Stokes, C. R., Murton, J. B., and Manica, A.: The configuration of Northern Hemisphere ice sheets through the Quaternary, Nat. Commun., 10, 3713, https://doi.org/10.1038/s41467-019-11601-2, 2019.

Bateman, M. D., Bryant, R. G., and Luo, W.: Getting the right age? Testing luminescence dating of both quartz and feldspars against independent age controls, Quat. Geochronol., 72, 101366, https://doi.org/10.1016/j.quageo.2022.101366, 2022.

Bateman, M. D., Kinnaird, T. C., Hill, J., Ashurst, R. A., Mohan, J., Bateman, R. B. I., and Robinson, R.: Detailing the impact of the Storegga Tsunami at Montrose, Scotland, Boreas, 50, 1059–1078, https://doi.org/10.1111/bor.12532, 2021.

Birnie, J.: Environmental changes in Shetland since the end of the last glaciation, Doctoral dissertation, University of Aberdeen, 1981.

Bondevik, S., Inge Svendsen, J., and Mangerud, J.: Tsunami sedimentary facies deposited by the Storegga tsunami in shallow marine basins and coastal lakes, western Norway, Sedimentology, 44, 1115–1131, https://doi.org/10.1046/j.1365-3091.1997.d01-63.x, 1997.

Bondevik, S., Mangerud, J., Dawson, S., Dawson, A., and Lohne, Ø.: Record-breaking height for 8000-year-old tsunami in the North Atlantic, Eos, 84, 289–300, https://doi.org/10.1029/2003EO310001, 2003.

Bondevik, S., Mangerud, J., Dawson, S., Dawson, A., and Lohne, Ø.: Evidence for three North Sea tsunamis at the Shetland Islands between 8000 and 1500 years ago, Quat. Sci. Rev., 24, 1757–1775, https://doi.org/10.1016/j.quascirev.2004.10.018, 2005.

Bondevik, S., Stormo, S. K., and Skjerdal, G.: Green mosses date the Storegga tsunami to the chilliest decades of the 8.2 ka cold event, Quat. Sci. Rev., 45, 1–6, https://doi.org/10.1016/j.quascirev.2012.04.020, 2012.

Bøtter-Jensen, L., and Mejdahl, V.: Determination of potassium in feldspars by beta counting using a GM multicounter system, Nucl. Tracks Radiat. Meas., 10, 663–666, https://doi.org/10.1016/0735-245X(85)90073-0, 1985.

Bøtter-Jensen, L., and Mejdahl, V.: Assessment of beta dose-rate using a GM multicounter system, Int. J. Radiat. Appl. Instrum. Part D: Nucl. Tracks Radiat. Meas., 14, 187–191, https://doi.org/10.1016/1359-0189(88)90062-3, 1988.

Bradley, S. L., Milne, G. A., Shennan, I., and Edwards, R.: An improved glacial isostatic adjustment model for the British Isles, J. Quat. Sci., 26, 541–552, https://doi.org/10.1002/jqs.1481, 2011.

Bradley, S. L., Ely, J. C., Clark, C. D., Edwards, R. J., and Shennan, I.: Reconstruction of the palaeo-sea level of Britain and Ireland arising from empirical constraints of ice extent: implications for regional sea level forecasts and North American ice sheet volume, J. Quat. Sci., 38, 791–805, https://doi.org/10.1002/jqs.3523, 2023.

Bradwell, T., Small, D., Fabel, D., Clark, C. D., Chiverrell, R. C., Saher, M. H., Dove, D., Callard, S. L., Burke, M. J., Moreton, S. G., Medialdea, A., Bateman, M. D., Roberts, D. H., Golledge, N. R., Finlayson, A., Morgan, S., and Cofaigh, C. Ó.: Pattern, style and timing of British–Irish Ice Sheet retreat: Shetland and northern North Sea sector, J. Quat. Sci., 36, 681–722, https://doi.org/10.1002/jqs.3163, 2019.

https://doi.org/10.5194/egusphere-2026-3279
Preprint. Discussion started: 3 September 2026

Brennan, B. J.: Beta doses to spherical grain, Radiat. Meas., 37, 299–303, https://doi.org/10.1016/S1350-4487(03)00011-8, 2003.

Brennan, B. J., Lyons, R. G., and Phillips, S. W.: Attenuation of alpha particle track dose for spherical grains, Int. J. Radiat. Appl. Instrum. Part D: Nucl. Tracks Radiat. Meas., 18, 249–253, https://doi.org/10.1016/1359-0189(91)90119-3, 1991.

Brill, D., and Tamura, T.: Optically stimulated luminescence dating of tsunami and storm deposits, in: Engel, M., Pilarczyk, J., May, S. M., Brill, D., and Garrett, E. (Eds.), Geological Records of Tsunamis and Other Extreme Waves. Elsevier, pp. 705–727, https://doi.org/10.1016/B978-0-12-815686-5.00032-8, 2020.

Brill, D., Klasen, N., Jankaew, K., Brückner, H., Kelletat, D., Scheffers, A., and Scheffers, S.: Local inundation distances and regional tsunami recurrence in the Indian Ocean inferred from luminescence dating of sandy deposits in Thailand, Nat. Hazards Earth Syst. Sci., 12, 2177–2192, https://doi.org/10.5194/nhess-12-2177-2012, 2012.

Brill, D., Reimann, T., Wallinga, J., May, S. M., Engel, M., Riedesel, S., and Brückner, H.: Testing the accuracy of feldspar single grains to date late Holocene cyclone and tsunami deposits, Quat. Geochronol., 48, 91–103, https://doi.org/10.1016/j.quageo.2018.09.001, 2018.

Brill, D., Zander, A., Costa, P., Feist, L., Laermanns, H., Reicherter, K., and Brückner, H.: Luminescence dating of tsunami deposits from the Algarve shelf, Portugal, Quat. Geochronol., 81, 101513, https://doi.org/10.1016/j.quageo.2024.101513, 2024.

Bronk Ramsey, C.: Deposition models for chronological records, Quat. Sci. Rev., 27, 42–60, https://doi.org/10.1016/j.quascirev.2007.01.019, 2008.

Bronk Ramsey, C.: Bayesian Analysis of Radiocarbon Dates, Radiocarbon, 51, 337–360, https://doi.org/10.1017/S0033822200033865, 2009.

Bryn, P., Berg, K., Forsberg, C. F., Solheim, A., and Kvalstad, T. J.: Explaining the Storegga Slide, Mar. Pet. Geol., 22, 11–19, https://doi.org/10.1016/j.marpetgeo.2004.12.003, 2005.

Buylaert, J. P., Murray, A. S., Thomsen, K. J., and Jain, M.: Testing the potential of an elevated temperature IRSL signal from K-feldspar, Radiat. Meas., 44, 560–565, https://doi.org/10.1016/j.radmeas.2009.02.007, 2009.

Cain, G., Goff, J., and McFadgen, B.: Prehistoric coastal mass burials: Did death come in waves?, J. Archaeol. Method Theory, 26, 714–754, https://doi.org/10.1007/s10816-018-9386-y, 2019.

Chagué, C.: Applications of geochemical proxies in paleotsunami research, in: Engel, M., Pilarczyk, J., May, S. M., Brill, D., and Garrett, E. (Eds.), Geological Records of Tsunamis and Other Extreme Waves. Elsevier, pp. 381–401, https://doi.org/10.1016/B978-0-12-815686-5.00018-3, 2020.

Chamberlain, E. L., Wallinga, J., Reimann, T., Goodbred, S. L., Steckler, M. S., Shen, Z., and Sincavage, R.: Luminescence dating of delta sediments: Novel approaches explored for the Ganges-Brahmaputra-Meghna Delta, Quat. Geochronol., 41, 97–111, https://doi.org/10.1016/j.quageo.2017.06.006, 2017.

Chamberlain, E. L., Wallinga, J., and Shen, Z.: Luminescence age modeling of variably-bleached sediment: Model selection and input, Radiat. Meas., 120, 221–227, https://doi.org/10.1016/j.radmeas.2018.06.007, 2018.

Costa, P., Dawson, S., Ramalho, R., Engel, M., Dourado, F., Bosnic, I., and Andrade, C.: A review on onshore tsunami deposits along the Atlantic coasts, Earth-Sci. Rev., 212, 103441, https://doi.org/10.1016/j.earscirev.2020.103441, 2021a.

Costa, P. J. M., Feist, L., Dawson, A. G., Stewart, I., Reicherter, K., and Andrade, C.: An overview on offshore tsunami deposits, in: Shiki, T., Tsuji, Y., Yamazaki, T., and Nanayama, E. (Eds.), Tsunamiites. Elsevier, pp. 183–192, https://doi.org/10.1016/B978-0-12-823939-1.00011-2, 2021b.

https://doi.org/10.5194/egusphere-2026-3279
Preprint. Discussion started: 3 September 2026

Cunningham, A., Tamura, T., and Armitage, S.: Applications in coastal and marine environments, in: Bateman, M. (Ed.), Handbook of Luminescence Dating, Whittles Publishing, Caithness, pp. 259–292, 2019.

Cuven, S., Paris, R., Falvard, S., Miot-Noirault, E., Benbakkar, M., Schneider, J.-L., and Billy, I., 2013. High-resolution analysis of a tsunami deposit: Case study from the 1755 Lisbon tsunami in southwestern Spain, Mar. Geol., 337, 98–111, https://doi.org/10.1016/j.margeo.2013.02.002, 2013.

Dawson, A. G., and Stewart, I.: Tsunami deposits in the geological record, Sediment. Geol., 200, 166–183, https://doi.org/10.1016/j.sedgeo.2007.01.002, 2007.

Dawson, A., Dawson, S., and Bondevik, S.: A late Holocene Tsunami at Basta Voe, Yell, Shetland Isles, Scott. Geogr. J., 122, 100–108, https://doi.org/10.1080/00369220618737258, 2006.

Dawson, A. G., Dawson, S., Bondevik, S., Costa, P. J. M., Hill, J., and Stewart, I.: Reconciling Storegga tsunami sedimentation patterns with modelled wave heights: A discussion from the Shetland Isles field laboratory, Sedimentology, 67, 1344–1353, https://doi.org/10.1111/sed.12643, 2020.

Dawson, S., and Smith, D. E.: The sedimentology of Middle Holocene tsunami facies in northern Sutherland, Scotland, UK, Mar. Geol., 170, 69–79, https://doi.org/10.1016/S0025-3227(00)00066-9, 2000.

Dawson, S., Costa, P., Dawson, A., and Engel, M.: Onshore archives of tsunami deposits, in: Engel, M., Pilarczyk, J., May, S. M., Brill, D., and Garrett, E. (Eds.), Geological Records of Tsunamis and Other Extreme Waves. Elsevier, pp. 95–111, https://doi.org/10.1016/B978-0-12-815686-5.00006-7, 2020.

Degering, D., and Degering, A.: Change is the only constant - time-dependent dose rates in luminescence dating, Quat. Geochronol., 58, 101074, https://doi.org/10.1016/j.quageo.2020.101074, 2020.

Devendra, D., Łącka, M., Szymańska, N., Nethupul, H., Pawłowska, J., Szymczak-Żyła, M., Krajewska, M., De Silva, P., Bondevik, S., Gibbons, S. J., and Zajączkowski, M.: Expanding the footprint of the Storegga tsunami through new evidence from Arctic marine sediments, Sci. Rep., 15, 24809, https://doi.org/10.1038/s41598-025-10811-7, 2025.

Earland, J. L., Scourse, J. D., Ehmen, T., Kender, S., and Ascough, P.: Identification of the Storegga event offshore Shetland, Mar. Geol., 474, 107334, https://doi.org/10.1016/j.margeo.2024.107334, 2024.

Engel, M., May, S. M., Pilarczyk, J., Brill, D., and Garrett, E.: Geological records of tsunamis and other extreme waves: concepts, applications and a short history of research, in: Geological Records of Tsunamis and Other Extreme Waves. Elsevier, pp. 3–20, https://doi.org/10.1016/B978-0-12-815686-5.00001-8, 2020.

Engel, M., Hess, K., Dawson, S., Patel, T., Koutsodendris, A., Vakhrameeva, P., Klemt, E., Kempf, P., Schön, I., and Heyvaert, V. M. A.: Sedimentary evidence of the Late Holocene tsunami in the Shetland Islands (UK) at Loch Flugarth, northern Mainland, Boreas, 53, 27–41, https://doi.org/10.1111/bor.12635, 2024.

Falvard, S., and Paris, R.: X-ray tomography of tsunami deposits: Towards a new depositional model of tsunami deposits, Sedimentology, 64, 453–477, https://doi.org/10.1111/sed.12310, 2017.

Feist, L., Costa, P. J. M., Bellanova, P., Bosnic, I., Santisteban, J. I., Andrade, C., Brückner, H., Duarte, J. F., Kuhlmann, J., Schwarzbauer, J., Vött, A., and Reicherter, K.: Holocene offshore tsunami archive – Tsunami deposits on the Algarve shelf (Portugal), Sediment. Geol., 448, 106369, https://doi.org/10.1016/j.sedgeo.2023.106369, 2023.

Fruergaard, M., Piasecki, S., Johannessen, P. N., Noe-Nygaard, N., Andersen, T. J., Pejrup, M., and Nielsen, L. H.: Tsunami propagation over a wide, shallow continental shelf caused by the Storegga slide, southeastern North Sea, Denmark, Geology, 43, 1047–1050, https://doi.org/10.1130/G37151.1, 2015.

Gaffney, V., Fitch, S., Bates, M., Ware, R. L., Kinnaird, T., Gearey, B., Hill, T., Telford, R., Batt, C., Stern, B., Whittaker, J., Davies, S., Sharada, M. B., Everett, R., Cribdon, R., Kistler, L., Harris, S., Kearney, K., Walker, J., Muru, M., Hamilton, D.,

https://doi.org/10.5194/egusphere-2026-3279
Preprint. Discussion started: 3 September 2026

Law, M., Finlay, A., Bates, R., and Allaby, R. G.: Multi-proxy characterisation of the Storegga Tsunami and its impact on the Early Holocene landscapes of the southern North Sea, Geosciences, 10, 270, https://doi.org/10.3390/geosciences10070270, 2020.

Galbraith, R. F.: Statistics for Fission Track Analysis, Chapman and Hall/CRC, New York, https://doi.org/10.1201/9781420034929, 2005.

Galbraith, R. F., Roberts, R. G., Laslett, G. M., Yoshida, H., and Olley, J. M.: Optical dating of single and multiple grains of quartz from Jinmium Rock Shelter, northern Australia: Part I, experimental design and statistical models, Archaeometry, 41, 339–364, https://doi.org/10.1111/j.1475-4754.1999.tb00987.x, 1999.

GEBCO Compilation Group: The GEBCO_2025 Grid – a continuous terrain model of the global oceans and land at 15 arc-second intervals, NERC EDS British Oceanographic Data Centre NOC, https://doi.org/doi:10.5285/37c52e96-24ea-67ce-e063-7086abc05f29, 2025.

Godfrey-Smith, D. I., Huntley, D. J., and Chen, W.-H.: Optical dating studies of quartz and feldspar sediment extracts. Quat. Sci. Rev., 7, 373–380, https://doi.org/10.1016/0277-3791(88)90032-7, 1988.

Goodman-Tchernov, B., Dey, H., Reinhardt, E., McCoy, F., and Mart, Y.: Tsunami waves generated by the Santorini eruption reached Eastern Mediterranean shores, Geology, 37, 943–946, https://doi.org/10.1130/g25704a.1, 2009.

Graham, A. G. C., Stoker, M. S., Lonergan, L., Bradwell, T., and Stewart, M. A.: The Pleistocene glaciations of the North Sea basin, Dev. Quat. Sci., 15, 261–278, https://doi.org/10.1016/B978-0-444-53447-7.00021-0, 2011.

Grauert, M., Björck, S., and Bondevik, S.: Storegga tsunami deposits in a coastal lake on Suðuroy, the Faroe Islands, Boreas, 30, 263–271, https://doi.org/10.1111/j.1502-3885.2001.tb01045.x, 2001.

Guérin, G., Mercier, N., and Adamiec, G.: Dose-rate conversion factors: Update, Ancient TL, 29, 5–8, https://doi.org/10.26034/la.atl.2011.443, 2011.

Haflidason, H., Lien, R., Sejrup, H., Forsberg, C., and Bryn, P.: The dating and morphometry of the Storegga Slide, Mar. Pet. Geol., 22, 123–136, https://doi.org/10.1016/j.marpetgeo.2004.10.008, 2005.

Hall, A. M., Hansom, J. D., and Gordon, J. E.: Shetland, in: Ballantyne, C. K., and Gordon, J. E. (Eds.), Landscapes and Landforms of Scotland, Springer, Cham, pp. 135–150, https://doi.org/10.1007/978-3-030-71246-4_7, 2021.

Hess, K., Engel, M., Patel, T., Vakhrameeva, P., Koutsodendris, A., Klemt, E., Hansteen, T. H., Kempf, P., Dawson, S., Schön, I., and Heyvaert, V. M. A.: A 1500-year record of North Atlantic storm flooding from lacustrine sediments, Shetland Islands (UK), J. Quat. Sci., 39, 37–53, https://doi.org/10.1002/jqs.3568, 2024.

Hill, J., Avdis, A., Mouradian, S., and Collins, G.: Was Doggerland catastrophically flooded by the Mesolithic Storegga tsunami?, arXiv, https://doi.org/10.48550/arXiv.1707.05593, 2017.

Huntley, D. J., and Baril, M.R.: The K content of the K-feldspars being measured in optical dating or in thermoluminescence dating, Ancient TL, 15(1), 11–13, https://doi.org/10.26034/la.atl.1997.271, 1997.

Huntley, D. J., and Lamothe, M.: Ubiquity of anomalous fading in K-feldspars and the measurement and correction for it in optical dating, Can. J. Earth Sci., 38, 1093–1106, https://doi.org/10.1139/e01-013, 2001.

Karstens, J., Haflidason, H., Berndt, C., and Crutchley, C. J.: Revised Storegga Slide reconstruction reveals two major submarine landslides 12,000 years apart, Commun. Earth Environ., 4, 55, https://doi.org/10.1038/s43247-023-00710-y, 2023.

Kreutzer, S., Schmidt, C., DeWitt, R., and Fuchs, M.: The a-value of polymineral fine grain samples measured with the post-IR IRSL protocol, Radiat. Meas., 69, 18–29, https://doi.org/10.1016/j.radmeas.2014.04.027, 2014.

Kreutzer, S., Schmidt, C., Fuchs, Margret, Dietze, M., Fischer, M., and Fuchs, M.: Introducing an R package for luminescence dating analysis, Ancient TL, 30, 1–8, https://doi.org/10.26034/la.atl.2012.457, 2012.

Kuchar, J., Milne, G., Hubbard, A., Patton, H., Bradley, S., Shennan, I., and Edwards, R.: Evaluation of a numerical model of the British–Irish ice sheet using relative sea-level data: implications for the interpretation of trimline observations, J. Quat. Sci., 27, 597–605, https://doi.org/10.1002/jqs.2552, 2012.

Li, W., Li, X., Mei, X., Zhang, F., Xu, J., Liu, C., Wei, C., and Liu, Q.: A review of current and emerging approaches for Quaternary marine sediment dating, Sci. Total Environ., 780, 146522, https://doi.org/10.1016/j.scitotenv.2021.146522, 2021.

Long, D.: A catalogue of tsunamis reported in the UK. British Geological Survey, Edinburgh, https://nora.nerc.ac.uk/id/eprint/513298/ (last access: 29 May 2026), 2015.

Long, D., Dawson, A. G., and Smith, D. E.: Tsunami risk in northwestern Europe: a Holocene example, Terra Nova, 1, 532–537, https://doi.org/10.1111/j.1365-3121.1989.tb00429.x, 1989.

López, G. I., Goodman-Tchernov, B. N., and Porat, N.: OSL over-dispersion: A pilot study for the characterisation of extreme events in the shallow marine realm, Sediment. Geol., 378, 35–51, https://doi.org/10.1016/j.sedgeo.2018.09.002, 2018.

Mahan, S., Rittenour, T., Nelson, M., Ataee, N., Brown, N., DeWitt, R., Durcan, J., Evans, M., Feathers, J., Frouin, M., Guérin, G., Heydari, M., Huot, S., Jain, M., Keen-Zebert, A., Li, B., López, G., Neudorf, C., Porat, N., Rodrigues, K., Sawakuchi, A. O., Spencer, J. Q. G., and Thomsen, K.: Guide for interpreting and reporting luminescence dating results, Geol. Soc. Am. Bull., 135, 1480–1502, https://doi.org/10.1130/B36404.1, 2022.

Maßon, L. A. E., Riedesel, S., Opitz, S., Zander, A., Bell, A., Cieszynski, H., and Reimann, T.: How much K is OK? – Evaluating different methods for K-concentration determination and the effect of the internal K-concentration on feldspar luminescence dating, Geochronology, 7, 475–492, https://doi.org/10.5194/gchron-7-475-2025, 2025.

Murari, M. K., Achyuthan, H., and Singhvi, A. K.: Luminescence studies on the sediments laid down by the December 2004 tsunami event: prospects for the dating of palaeo tsunami events and for the estimation of sediment fluxes, Curr. Sci., 92, 367–371, 2007.

Murray, A., Arnold, L., Buylaert, J.-P., Guérin, G., Qin, J., Singhvi, A., Smedley, R., and Thomsen, K.: Optically stimulated luminescence dating using quartz, Nat. Rev. Methods Primers, 1, 72, https://doi.org/10.1038/s43586-021-00068-5, 2021.

Nentwig, V., Tsukamoto, S., Frechen, M., and Bahlburg, H.: Reconstructing the tsunami record in Tirúa, Central Chile beyond the historical record with quartz-based SAROSL, Quat. Geochronol., 30, 299–305, https://doi.org/10.1016/j.quageo.2015.05.020, 2015.

Neumann, B., Vafeidis, A. T., Zimmermann, J., and Nicholls, R. J.: Future coastal population growth and exposure to sea-level rise and coastal flooding – A global assessment, PLoS ONE, 10, e0118571, https://doi.org/10.1371/journal.pone.0118571, 2015.

Nielsen, S. V.: Wave? What wave? Testing for impact of the Garth tsunami (3500 BCE) on Neolithic coastal settlements in Western Norway, J. Archaeol. Sci. Rep., 33, 102464, https://doi.org/10.1016/j.jasrep.2020.102464, 2020.

Nussberger, N., Engel, M., Patel, T., Varychev, A., Meyer, H.-P., Brill, D., Pint, A., Kempf, P., Hess, K., Schön, I., Heyvaert, V. M. A., and Dawson, S.: Late Holocene tsunami hydrodynamics, sediment provenance and chronology from Dury Voe, Shetland Islands (UK), EarthArXiv, https://doi.org/10.31223/X55R3P, under review.

Peffeköver, A., Engel, M., Opitz, S., Zander, A., Van Daele, M., Costa P. J. M., Dawson, S., An Nahar, R. N. F., Scheder, J., Heyvaert, V. M. A., De Batist, M., and Brill, D.: Luminescence dating of offshore tsunami deposits from the Shetland Islands, United Kingdom, Zenodo [data set], https://doi.org/10.5281/zenodo.21363495, 2026.

Prescott, J. R., and Hutton, J. T.: Cosmic ray contributions to dose rates for luminescence and ESR dating: Large depths and long-term time variations, Radiat. Meas., 23, 497–500, https://doi.org/10.1016/1350-4487(94)90086-8, 1994.

Rasmussen, H., Bondevik, S., and Corner, G. D.: Holocene relative sea level history and Storegga tsunami run-up in Lyngen, northern Norway, J. Quat. Sci., 33, 393–408, https://doi.org/10.1002/jqs.3021, 2018.

Reimann, T., and Tsukamoto, S.: Dating the recent past (<500 years) by post-IR IRSL feldspar – Examples from the North Sea and Baltic Sea coast, Quat. Geochronol., 10, 180–187, https://doi.org/10.1016/j.quageo.2012.04.011, 2012.

Reinhardt, E., Goodman-Tchernov, B., Boyce, J., Van, P., Rink, W. J., Mart, Y., Raban, A., and López, G.: The tsunami of 13 December A.D. 115 and the destruction of Herod the Great's harbor at Caesarea Maritima, Israel, Geology, 34, 1061–1064, https://doi.org/10.1130/G22780A.1, 2006.

Rhodes, E. J., Bronk Ramsey, C., Outram, Z., Batt, C., Willis, L., Dockrill, S., and Bond, J.: Bayesian methods applied to the interpretation of multiple OSL dates: high precision sediment ages from Old Scatness Broch excavations, Shetland Isles, Quat. Sci. Rev., 22, 1231–1244. https://doi.org/10.1016/S0277-3791(03)00046-5, 2003.

Riedesel, S., Brill, D., Roberts, H. M., Duller, G. A. T., Garrett, E., Zander, A. M., King, G. E., Tamura, T., Burow, C., Cunningham, A., Seeliger, M., De Batist, M., Heyvaert, V. M. A., Fujiwara, O., and Brückner, H.: Single-grain feldspar luminescence chronology of historical extreme wave event deposits recorded in a coastal lowland, Pacific coast of central Japan, Quat. Geochronol., 45, 37–49, https://doi.org/10.1016/j.quageo.2018.01.006, 2018.

Romundset, A., and Bondevik, S.: Propagation of the Storegga tsunami into ice-free lakes along the southern shores of the Barents Sea. J. Quat. Sci., 26, 457–462, https://doi.org/10.1002/jqs.1511, 2011.

Romundset, A., Fredin, O., and Høgaas, F.: A Holocene sea-level curve and revised isobase map based on isolation basins from near the southern tip of Norway, Boreas, 44, 383–400, https://doi.org/10.1111/bor.12105, 2015.

Sawai, Y., Namegaya, Y., Okamura, Y., Satake, K., and Shishikura, M.: Challenges of anticipating the 2011 Tohoku earthquake and tsunami using coastal geology, Geophys. Res. Lett., 39, L21309, https://doi.org/10.1029/2012GL053692, 2012.

Schwarzer, K.: Geophysical prospection and sedimentological characteristics of subaquatic tsunami deposits, in: Engel, M., Pilarczyk, J., May, S. M., Brill, D., and Garrett, E. (Eds.), Geological Records of Tsunamis and Other Extreme Waves, Elsevier, pp. 115–142, https://doi.org/10.1016/B978-0-12-815686-5.00007-9, 2020.

Shennan, I., Bradley, S. L., and Edwards, R.: Relative sea-level changes and crustal movements in Britain and Ireland since the Last Glacial Maximum. Quat. Sci. Rev., 188, 143–159, https://doi.org/10.1016/j.quascirev.2018.03.031, 2018.

Smedley, R. K., Duller, G., Pearce, N., and Roberts, H.: Determining the K-content of single-grains of feldspar for luminescence dating, Radiat. Meas., 47, 790–796, https://doi.org/10.1016/j.radmeas.2012.01.014, 2012.

Smith, D. E.: Norwick, Unst; Burragarth, Unst; Sullom Voe, Mainland, in: Birnie, J., Gordon, J., Bennett, K., and Hall, A. M. (Eds.), The Quaternary of Shetland, Quaternary Research Association, London, 52–56, 1993.

Smith, D., Shi, S., Cullingford, R. A., Dawson, A. G., Dawson, S., Firth, C. R., Foster, I. D. L., Fretwell, P. T., Haggart, B. A., Holloway, L. K., and Long, D.: The Holocene Storegga Slide tsunami in the United Kingdom, Quat. Sci. Rev., 23, 2291–2321, https://doi.org/10.1016/j.quascirev.2004.04.001, 2004.

Solheim, A., Berg, K., Forsberg, C. F., and Bryn, P.: The Storegga Slide complex: repetitive large scale sliding with similar cause and development, Mar. Pet. Geol., 22, 97–107, https://doi.org/10.1016/j.marpetgeo.2004.10.013, 2005.

Spiske, M.: The sedimentology and geometry of fine-grained tsunami deposits from onshore environments, in: Engel, M., Pilarczyk, J., May, S. M., Brill, D., and Garrett, E. (Eds.), Geological Records of Tsunamis and Other Extreme Waves, Elsevier, pp. 213–238, https://doi.org/10.1016/B978-0-12-815686-5.00011-0, 2020.

https://doi.org/10.5194/egusphere-2026-3279
Preprint. Discussion started: 3 September 2026

Sugawara, D., Minoura, K., and Imamura, F.: Tsunamis and tsunami sedimentology, in: Tsunamiites: Features and Implications. Elsevier, pp. 9–51, https://doi.org/10.1016/B978-0-12-823939-1.00003-3, 2020.

Szczuciński, W.: Post-depositional changes to tsunami deposits and their preservation potential, in: Engel, M., Pilarczyk, J., May, S.M., Brill, D., and Garrett, E. (Eds.), Geological Records of Tsunamis and Other Extreme Waves, Elsevier, pp. 443–469, https://doi.org/10.1016/B978-0-12-815686-5.00021-3, 2020.

Tooley, M. J., and Smith, D.E.: Relative sea-level change and evidence for the Holocene Storegga Slide tsunami from a high-energy coastal environment: Cocklemill Burn, Fife, Scotland, UK, Quat. Int., 133–134, 107–119, https://doi.org/10.1016/j.quaint.2004.10.007, 2005.

Van Daele, M., Costa, P. J. M., Engel, M., An Nahar, R., Lisson, K., Goovaerts, T., Bertels, R., Meyvis, B., Teixeira, M., Dourado, F., Cavadas, H., Hess, K., Peffeköver, A., Bloume, W., Vermaut, J., Mesquita, Y., and Bautista, C.: RV Belgica 2023/16 Cruise Report (last access: 29 May 2026), https://odnature.naturalsciences.be/belgica_media/downloads/belgica/campaigns/reports/re2023_16.pdf, 2023.

Wagner, B., Bennike, O., Klug, M., and Cremer, H.: First indication of Storegga tsunami deposits from East Greenland, J. Quat. Sci., 22, 321–325, https://doi.org/10.1002/jqs.1064, 2007.

Wahl, T., Haigh, I. D., Woodworth, P. L., Albrecht, F., Dillingh, D., Jensen, J., Nicholls, R. J., Weisse, R., and Wöppelmann, G.: Observed mean sea level changes around the North Sea coastline from 1800 to present, Earth-Sci. Rev., 124, 51–67, https://doi.org/10.1016/j.earscirev.2013.05.003, 2013.

Watts, L. M., Holdsworth, R. E., Sleight, J. A., Strachan, R. A., and Smith, S. A. F.: The movement history and fault rock evolution of a reactivated crustal-scale strike-slip fault: the Walls Boundary Fault Zone, Shetland, J. Geol. Soc., 164, 1037–1058, https://doi.org/10.1144/0016-76492006-156, 2007.

Zander, A., Degering, D., Preusser, F., Kasper, H. U., and Brückner, H.: Optically stimulated luminescence dating of sublittoral and intertidal sediments from Dubai, UAE: Radioactive disequilibria in the uranium decay series, Quat. Geochronol., 2, 123–128, https://doi.org/10.1016/j.quageo.2006.04.003, 2007.